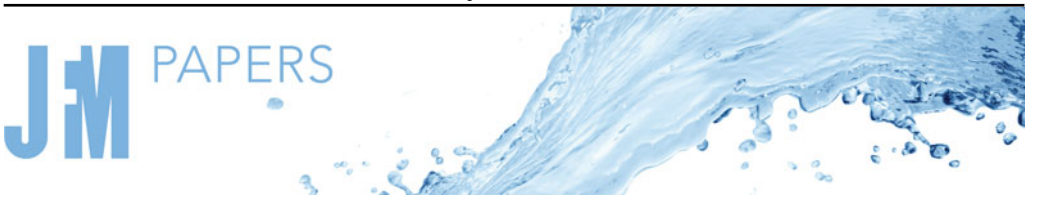
J. Fluid Mech. (2026), *vol.* 1039, A45, doi:10.1017/jfm.2026.11840



Dynamics of shear instabilities near the ice-shelf–ocean interface

Samuel G. Hartharn-Evans[1], **Charlie James Lloyd**[2], **Magda Carr**[3] and **Adrian Jenkins**[1]

[1]School of Geography and Natural Sciences, Northumbria University, Newcastle upon Tyne, UK
[2]School of Architecture, Building and Civil Engineering, Loughborough University, Loughborough, UK
[3]School of Mathematics, Statistics and Physics, Newcastle University, Newcastle upon Tyne, UK
Corresponding author: Samuel G. Hartharn-Evans, sam.hartharn-evans@northumbria.ac.uk

(Received 18 August 2025 UTC; revised 8 June 2026 UTC; accepted 18 June 2026 UTC)

The melting of ice shelves into the ocean plays a major role, and is a key source of uncertainty, in sea level rise projections. Under-ice shelves, meltwater moves upslope, setting up a stratified shear flow with the warmer, but critically saltier, ocean beneath, regulating the transfer of heat between ice and the ambient ocean. Such features are incredibly difficult to access *in situ*, and so most research has focussed on the use of numerical modelling, laboratory experiments and analytical models to understand these processes, each with their own trade-offs. Here, novel numerical simulations of the Navier–Stokes equations approximate this flow for a tilted domain forced with fixed densities at the upper and lower boundaries to induce such a buoyant boundary shear current. These simulations and accompanying linear stability analysis (LSA) reveal that the shear flows under-ice shelves form a unique mixed-mode shear instability. This instability consists of paired Kelvin Helmholtz and Holmboe instabilities, highly effective at mixing the water column, and due to the restoring effect of the boundary forcing, results in a cyclical instability. The flow criticality is found to be well predicted by LSA, and dependent on diagnostic flow Reynolds and bulk Richardson numbers, whilst the local gradient Richardson number is not a useful indicator of instability in this problem. Based on these results, it is unclear how well this unusual route to turbulent mixing is represented in current models, highlighting the need for further investigation into turbulent heat transfer and ice-shelf melting.

Key words: ice sheets, stratified flows, shear-flow instability

© The Author(s), 2026. Published by Cambridge University Press. This is an Open Access article, distributed under the terms of the Creative Commons Attribution licence (https://creativecommons.org/licenses/by/4.0/), which permits unrestricted re-use, distribution and reproduction, provided the original article is properly cited.

https://doi.org/10.1017/jfm.2026.11840 Published online by Cambridge University Press

1. Introduction

Over the past three decades, Antarctic ice loss has contributed 7.4 ± 1.47 mm to global mean sea level (Shepherd *et al.* 2018; Otosaka *et al.* 2023), and represents a major uncertainty in future sea level rise (Edwards *et al.* 2021; Hill *et al.* 2021; Fricker *et al.* 2025). Antarctic outflow glaciers, grounded on land, flow into the ocean, where they become floating ice shelves, and once floating, their mass contributes to the sea level. Ice shelves are eroded by a combination of thinning by ocean-driven melting from below and calving at the edges (Depoorter *et al.* 2013; Greene *et al.* 2022), processes that reduce their ability to restrain (buttress) the flow of ice sheets into the ocean (Fürst *et al.* 2016; Reese *et al.* 2018) and that are consequently the main cause of recent grounded ice losses over Antarctica (Pritchard *et al.* 2012; Rignot *et al.* 2013; Reese *et al.* 2018). Quantifying the rate at which ice shelves melt into the underlying ocean, now and in the future, is therefore an urgent challenge that must be tackled if we are to improve sea level projections (Edwards *et al.* 2021; Hill *et al.* 2021). The rate at which ice melts from below is critically dependent on mixing processes that bring deeper warm waters up towards the ice. Yet, the technical and logistical challenges of direct observations limit our current understanding of this process, leaving a critical knowledge gap.

Theoretical models (MacAyeal 1985; Jenkins 1991, 2021), large eddy simulations (Vreugdenhil & Taylor 2019; Begeman *et al.* 2022; Vreugdenhil *et al.* 2022; Anselin *et al.* 2024) and limited observations (Davis & Nicholls 2019; Rosevear, Galton-Fenzi & Stevens 2022; Davis *et al.* 2023; Schmidt *et al.* 2023) have indicated that, at the interface between the ocean and ice shelf, a stratified shear flow can form, regulating the vertical transfer of heat towards the ice. Freshwater released into the ocean by ice ablation is more buoyant than the ambient, salty (but relatively warm) ocean, and flows along the gently tilting underside of the ice shelf (figure 1*a*). This buoyant freshwater forms a stratification which means that fluid parcels perturbed vertically feel a restoring (buoyant) force, and the turbulent transport of scalars across stratified interfaces is suppressed. At the same time, the shear generated by this buoyant flow acts to produce turbulence and destabilise the flow, causing warm, salty ambient ocean water to entrain (mix) into the ice-shelf-adjacent meltwater-modified flow. In order to model the effect of this flow on ice melting in the real world, a fundamental understanding of the flow under idealised conditions is needed; however, there is currently no such fundamental understanding of this situation of a stratified shear instability developing in proximity to a constant buoyancy interface.

Motivated by such a geophysical setting, this paper uses numerical simulations at the laboratory scale to study a stratified shear flow that develops a unique instability under the following conditions:

(i) The density at the upper and lower boundaries is fixed at a constant value (Dirichlet boundary conditions), representing the boundary formed by the melting interface between the ice shelf (upper boundary) and far-field ocean (lower boundary).
(ii) The velocity at the upper and lower boundaries is 0 (no-slip boundary conditions), representing a solid upper interface (the ice shelf at the upper boundary). Matching lower interface boundary conditions are required by the model set-up, but this condition has little impact as it is far from any dynamic processes.
(iii) The domain is tilted, in effect, providing a gently sloping upper interface in a computationally efficient manner.
(iv) The domain is periodic in the along-slope (x) dimension, representing conditions far from a lateral boundary.

https://doi.org/10.1017/jfm.2026.11840 Published online by Cambridge University Press

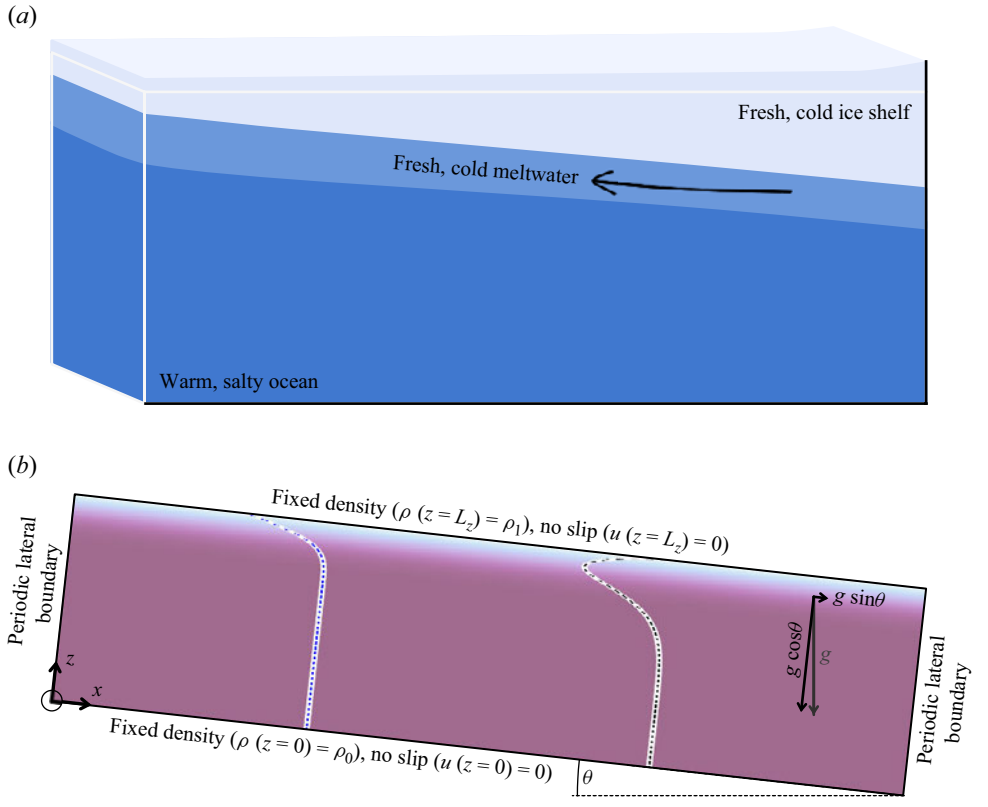


Figure 1. Schematic of (*a*) the ice-shelf–ocean boundary layer, where a fresh, cold meltwater-modified layer is formed from mixing of the warm, salty ocean with the fresher, colder products of ice-shelf melting. The upper layer propagates along the ice underside upslope. (*b*) Indicative density (ρ) profiles (background and blue/white line) and horizontal velocity (u) profiles (black/white line) from the growth phase of the buoyant boundary shear current. Direction of the gravity vector, g is shown.

Studying flows at this scale allows for the smallest scale of the dynamics that would be missed or parametrised in ocean models to be fully resolved. In turn, these simulations can provide insight into the calibration of sub-grid-scale models used in large eddy simulations (LES) and parameterisations in larger-scale ocean models.

In general, it is the balance between shear and stratification that determines where flow instability and associated mixing may occur. The relationship between shear and stratification can be characterised by the gradient Richardson number

$$Ri_g(z) \equiv \frac{-g}{\rho_0} \frac{\mathrm{d}\rho/\mathrm{d}z}{(\mathrm{d}u/\mathrm{d}z)^2}, \tag{1.1}$$

where g is the gravitational acceleration, ρ_0 a reference density, $\mathrm{d}\rho/\mathrm{d}z$ the vertical density gradient and $\mathrm{d}u/\mathrm{d}z$ the vertical gradient in the streamwise (along-slope) velocity, and where the condition $Ri_g < 1/4$ is a necessary, but not sufficient criterion for shear instability to occur (Miles 1961). Under idealised conditions, stratified shear flows are categorised into three canonical unstable modes. Firstly, the Kelvin–Helmholtz instability (KHI) (Helmholtz 1868; Kelvin 1871) describes flow where the interface rolls up into spiralling billows, where density interfaces overturn and mixing occurs by convective and secondary instabilities. Secondly, the Holmboe wave instability (HWI) describes a flow where the stratified interface is continually scoured away (Holmboe 1962). The final of

https://doi.org/10.1017/jfm.2026.11840 Published online by Cambridge University Press

these modes, the Taylor–Caulfield instability (Taylor 1931; Caulfield *et al.* 1995) is not relevant for this study, but is fully described in Eaves & Balmforth (2019). In each case, mixing characteristics of the flow are uniquely determined by overturning, scouring and the development of secondary and/or convective instabilities that can transition the flow to a turbulent state.

Our focus on under-ice meltwater flows is motivated by the occurrence of an unusual combination of characteristics that shape the flow and control the development of instability into a mixed-mode instability. Because of the gentle boundary slope, the stratification that develops adjacent to it is a source of both static stability and dynamic instability because of the sheared flow that develops (figure 1). Forcing on the flow arises from the buoyancy generated at the boundary itself, so is strongest at the boundary and decays away from it. Meanwhile, velocity shear is generated through both the sloping isopycnals and viscous drag, since the meltwater flows along a solid boundary, and the far-field velocity is zero in quiescent regions with no background or tidal currents. This differs from canonical boundary layer structures where a far-field velocity decays monotonically to zero at the boundary. A complex relationship exists between shear and buoyancy profiles that evolves with distance from the interface, while the development of instability is influenced by the proximity of the boundary. In the present study we leave aside other features of real-world, under-ice flows. These complexities could include implementing two buoyancy-determining properties, temperature and salinity, which have widely differing diffusivities and are both influenced by melting; and the rapid planetary rotation of the Earth. Instead, we focus on the fundamentals of the interplay between buoyancy and shear profiles and how the resulting instabilities develop in proximity to the solid boundary.

This work explores the fundamental dynamics of an unusual but nevertheless important class of flows, which develop in specific geophysical settings such as under melting ice shelves or where the atmospheric boundary layer is cooled over a sloping terrain (the process that gives rise to katabatic winds). We make use of idealised laboratory-scale numerical simulations (described in § 2.1) of a tilted rectangular domain (described in section § 2.2), alongside linear stability analysis (described in § 2.3) of profiles from the numerical simulations. In § 3, the dynamics of the idealised ice–ocean flow are presented from growth of the buoyant boundary shear current (§ 3.1), through primary (§ 3.2) and secondary instability phases (§3.3) to the long-term evolution of the flow. A mechanistic explanation of the flow (§ 3.2.3) is discussed. Finally, the implication of these results is discussed (§ 4), specifically what these results indicate about marginal instability in meltwater flows beneath ice shelves.

2. Methods

2.1. *Numerical model (SPINS)*

Numerical simulations were carried out with the pseudospectral code SPINS described by Subich, Lamb & Stastna (2013), designed to simulate stratified fluids with high (spectral) accuracy and efficiency when parallelised. The model solves the stratified incompressible Navier–Stokes equations subject to the Boussinesq approximation

$$\frac{\partial \boldsymbol{u}}{\partial t} + \boldsymbol{u}\cdot\nabla\boldsymbol{u} = -\frac{1}{\rho_0}\nabla P + \nu\nabla^2\boldsymbol{u} - \frac{\rho g}{\rho_0}\hat{e}_g, \tag{2.1}$$

$$\nabla\cdot\boldsymbol{u} = 0, \tag{2.2}$$

https://doi.org/10.1017/jfm.2026.11840 Published online by Cambridge University Press

$$\frac{\partial \rho}{\partial t} + \boldsymbol{u} \cdot \nabla \rho = \kappa \nabla^2 \rho, \tag{2.3}$$

where $\boldsymbol{u}$ is the velocity, t is time, P is the pressure, ρ is the density and ρ_0 is the reference density of the fluid $1000\,\mathrm{kg\,m^{-3}}$. The physical parameters are gravity g (set at $9.81\ \mathrm{ms}^{-2}$), the shear viscosity ν (set at $10^{-6}\mathrm{m}^2\mathrm{s}^{-1}$, unless otherwise stated, chosen to be consistent with the physical value) and the scalar diffusivity κ set so that the Schmidt number, $Sc = \nu/\kappa = 7$ for all cases (equivalent to the molecular value of $Pr = \nu/\kappa$ for temperature (Nayar *et al.* 2016)). The unit vector in the vertical direction is denoted by $\hat{e}_g$. The model solves the equations using a spectral collocation method, using a third-order multi-step method developed to allow adaptive time steps. An exponential filter is used to ensure numerical stability near the grid scale according to default settings (see Subich *et al.* 2013,for details).

The code has been thoroughly validated using theoretical results and physical laboratory experiments in a number of different configurations including shear instabilities (Subich *et al.* 2013), boundary layer instabilities (e.g. Harnanan, Stastna & Soontiens 2017), interaction with topography (e.g. Deepwell *et al.* 2017) and shoaling internal solitary waves (e.g. Hartharn-Evans *et al.* 2022). It is available for download through its online manual: https://wiki.math.uwaterloo.ca/fluidswiki/index.php?title=SPINS_User_Guide.

2.2. *Case set-up and experimental design*

The numerical tank is an initially two-dimensional (2-D) rectangular (unmapped) domain with length $L = 1$ m, and depth $H = 0.3$ m. One simulation is extended for 3-D simulation in § 3.3. Sloping upper and lower boundaries were implemented by 'tilting' the domain, adding a term to $\hat{e}$ in the buoyancy forcing term in (2.1) of the form $\hat{e} = (-\sin\theta, \cos\theta)$. Since the grids remain oriented with the boundaries of the tank, this method remains computationally efficient by avoiding the need for a mapped grid. Throughout this paper, references to the streamwise and vertical directions strictly refer to the x-axis (along the tank) and z-axis (vertical in the frame of the tank) (figure 1*a*). Periodic boundary conditions were applied in the streamwise (x) direction. Grid resolution in the x dimension was a uniformly spaced $N_x = 1024$ points, giving $\mathrm{d}x = 0.98$ mm. Both 2-D and 3-D simulations were carried out without Coriolis rotation.

Numerical simulations were carried out with no-slip boundary conditions (see table 1) at the upper and lower boundaries and employed a Chebyshev grid in the vertical, implying a clustering of points near both the upper and lower boundaries that scales with the number of points in the vertical squared. For these simulations, grid resolution in the vertical was $N_z = 512$, giving variable $\mathrm{d}z$ between $2.8\,\mu$m at the upper and lower boundaries and $920\,\mu$m near mid-depth, such that the region of the tank that becomes turbulent has high vertical resolution. We demonstrated mesh independence in Appendix A.

Upper boundary conditions representing the ice–ocean boundary were implemented via Dirichlet (fixed value) vertical boundary conditions for density

$$\rho(z = 0) = \rho_0, \tag{2.4}$$

$$\rho(z = H) = \rho_1. \tag{2.5}$$

An initial density profile was set using a very thin tanh profile to meet the smoothness condition for the spectral model at initialisation

$$\rho(z) = \rho_0 + \frac{\Delta\rho}{2}\left(1 - \tanh\left(\frac{2\left(z - (H - z_{pyc})\right)}{h_{pyc}}\right)\right), \tag{2.6}$$

https://doi.org/10.1017/jfm.2026.11840 Published online by Cambridge University Press

	$\Delta\rho$ (kg m^{-3})	θ (°)	ν (m^{2}s^{-1})
ISO_Base,	10	2	10^{-6}
ISO_0.5x_rho	**5**	2	10^{-6}
ISO_2x_rho	**20**	2	10^{-6}
ISO_5_slope,	10	**5**	10^{-6}
ISO_10_slope	10	**10**	10^{-6}
ISO_2x_ν	10	2	$\mathbf{2 \times 10^{-6}}$
ISO_0.5x_ν	10	2	$\mathbf{5 \times 10^{-7}}$

Table 1. Parameters for simulations used in this paper; density difference $\Delta\rho$, slope θ and viscosity ν. Parameters that differ from those in ISO_Base are highlighted in bold.

where $\Delta\rho = \rho_0 - \rho_1$ is the density difference, z_{pyc} the pycnocline location (distance beneath the upper interface) and h_{pyc} is the pycnocline thickness. Both h_{pyc} and z_{pyc} are set throughout these simulations at 0.001 m to be as small as possible whilst maintaining the smoothness criteria in initial conditions (identified via test simulations). In figure 5*a*, we show these profiles evolve in line with the expected analytic profiles, showing the simulations are insensitive to the initial condition.

The velocity profiles $u(z), w(z)$ were initialised at rest with small white noise perturbations (with amplitude of 10^{-3}) added at the initialisation of all simulations to trigger instability.

Simulations carried out are summarised in table 1, where prefixes of ISO (and throughout this paper) refer to ice-shelf–ocean simulations. Unless otherwise stated, results in the ensuing sections are based on ISO_Base, with additional sensitivity simulations presented later.

2.3. *Linear stability analysis*

By applying theoretical approaches to the outputs of time-resolved numerical simulations, fundamental processes driving the dynamics can be understood and identified. In particular, we aim to understand the stability of the time-evolving flow through the use of linear stability analysis (LSA), linearising about snapshots of the slowly evolving 2-D simulation profiles, averaged in x. The 2-D simulation profiles are essentially one-dimensional until instabilities grow and dominate the flow; averaging in x is performed to mitigate these small-scale instabilities to enable LSA to provide reasonable predictions during the early stages of unstable growth.

The implicit assumption here is that LSA solutions are valid when the flow evolution is slow compared with the growth rate of instabilities. In other words, once unstable growth begins in the simulations, it dominates over other flow evolution driven by either gravity or diffusion. The validity of these assumptions will be shown in § 3.2.1.

The base flow profiles at time t are denoted $\boldsymbol{U}(z) = (U(z), 0, 0)$, for velocity where $U(z) = \langle (u(x, z)\rangle_x$, $P(z) = \langle P\rangle_x$ for pressure and $B(z) = -\langle \rho(x, z)g/\rho_0\rangle_x$ for buoyancy, where $\langle\rangle_x$ represents averaging in the streamwise direction. Perturbations to these base flow profiles are given by $\boldsymbol{u}'$, p' and b'. Following the procedure outlined in Drazin & Reid (2004), Liu, Thorpe & Smyth (2012) and Lian, Smyth & Liu (2020), linearised equations can be formulated depending only on the vertical velocity and buoyancy perturbations. General normal-mode solutions are subsequently sought of the form $w' = \hat{w}(z)\exp(ik_x x + \lambda t)$ and $b' = \hat{b}(z)\exp(ik_x x + \lambda t)$, allowing for a general vertical

https://doi.org/10.1017/jfm.2026.11840 Published online by Cambridge University Press

dependence of the complex amplitudes or eigenfunctions $\hat{w}$ and $\hat{b}$. Here, k_x represents the streamwise wavenumber, and $\lambda = \sigma - i\omega$ represents a complex growth rate or eigenvalue related to the real growth rate σ and the temporal frequency ω. Consistent with the simulations, we restrict our analysis to 2-D modes with $k_y = 0$. Substitution into and manipulation of the governing equations leads to the viscous Taylor Goldstein (vTG) eigenvalue problem (Liu *et al.* 2012; Lloyd *et al.* 2022; Lloyd & Dorrell 2024)

$$\lambda \begin{bmatrix} \Delta & 0 \\ 0 & I \end{bmatrix} \begin{bmatrix} \hat{w} \\ \hat{b} \end{bmatrix} = \begin{bmatrix} -ik_x U\Delta + ik_x \dfrac{\mathrm{d}^2 U}{\mathrm{d}z^2} + \widehat{D}_w & -k_x^2 \\ -\dfrac{\mathrm{d}B}{\mathrm{d}z} & -ik_x U + \widehat{D}_b \end{bmatrix} \begin{bmatrix} \hat{w} \\ \hat{b} \end{bmatrix}, \tag{2.7}$$

where I represents the identity matrix, $\Delta = (\mathrm{d}^2/\mathrm{d}z^2) - k_x^2$ and the diffusive operators are defined as

$$\widehat{D}_w = \nu \left(k_x^4 - k_x^2 \frac{\mathrm{d}^2}{\mathrm{d}z^2} + \frac{\mathrm{d}^4}{\mathrm{d}z^4} \right) \quad \text{and} \quad \widehat{D}_b = \kappa \left(-k_x^2 + \frac{\mathrm{d}^2}{\mathrm{d}z^2} \right). \tag{2.8}$$

Note that we have neglected the streamwise component of the gravity unit vector $\boldsymbol{k}$ due to the low slope angles ($\theta < \sin\theta \ll \cos\theta$), where the destabilising effect of $\sin\theta$ on the streamwise component is negligible (Atoufi *et al.* 2023).

For a given wavenumber k_x, and specified profiles of U and B, the differential eigenvalue problem (2.7) can be (numerically) solved to obtain the complex growth rates (eigenvalues) λ and associated structure functions (eigenvectors) $\hat{w}$ and $\hat{b}$. The eigenvalue problem (2.7) is numerically solved, with discrete operators derived using Chebyshev polynomials with a resolution of $N_z = 128$ grid points (note that solutions are insensitive to further increase in resolution). Six boundary conditions are required to close the system. Consistent with the nonlinear simulation boundary conditions we specify $\hat{w} = 0$, $\hat{w}_z = 0$ and $\hat{b} = 0$ at the lower and upper boundaries, implemented using a 'give-back' matrix, following the procedure outlined by Lian *et al.* (2020).

Every 10 s of compute time we take the planar-averaged profiles from simulations and compute vTG solutions, using a robust peak-finding algorithm to maximise the growth rate σ and its corresponding wavenumber k_x. After some *a priori* testing we find that the maximum growth rates occur with $k_x \approx 18$. To find the precise k_x that maximises σ, to within two decimal places, we first adopt a coarse k_x grid between 0 and 30, then iteratively refine using a bisection method.

As we will show in § 3.2.1, the assumptions made for LSA produce modal structures, wavelengths and growth rates in excellent agreement with full numerical simulations.

3. Flow characteristics

3.1. *Time-evolving base flows*

After initialisation at rest, buoyancy (low density) diffuses from the upper boundary, which forms a continually stratified layer, the depth of which increases entirely by diffusion of density down the density gradient (figure 2*a*). The density evolves in a way that is insensitive to the initial condition (beyond a requirement for a smooth, thin transition), quickly deviating in form from the tanh profile ((2.6), figure 2*a*) to an error function. The density interface consists of a quasi-linearly stratified layer at the upper surface, overlaying a well-mixed lower layer (figures 2*a* and 2*e*). This density gradient weakens over time as the depth of the stratified layer increases (without a corresponding increase in magnitude of the density difference).

https://doi.org/10.1017/jfm.2026.11840 Published online by Cambridge University Press

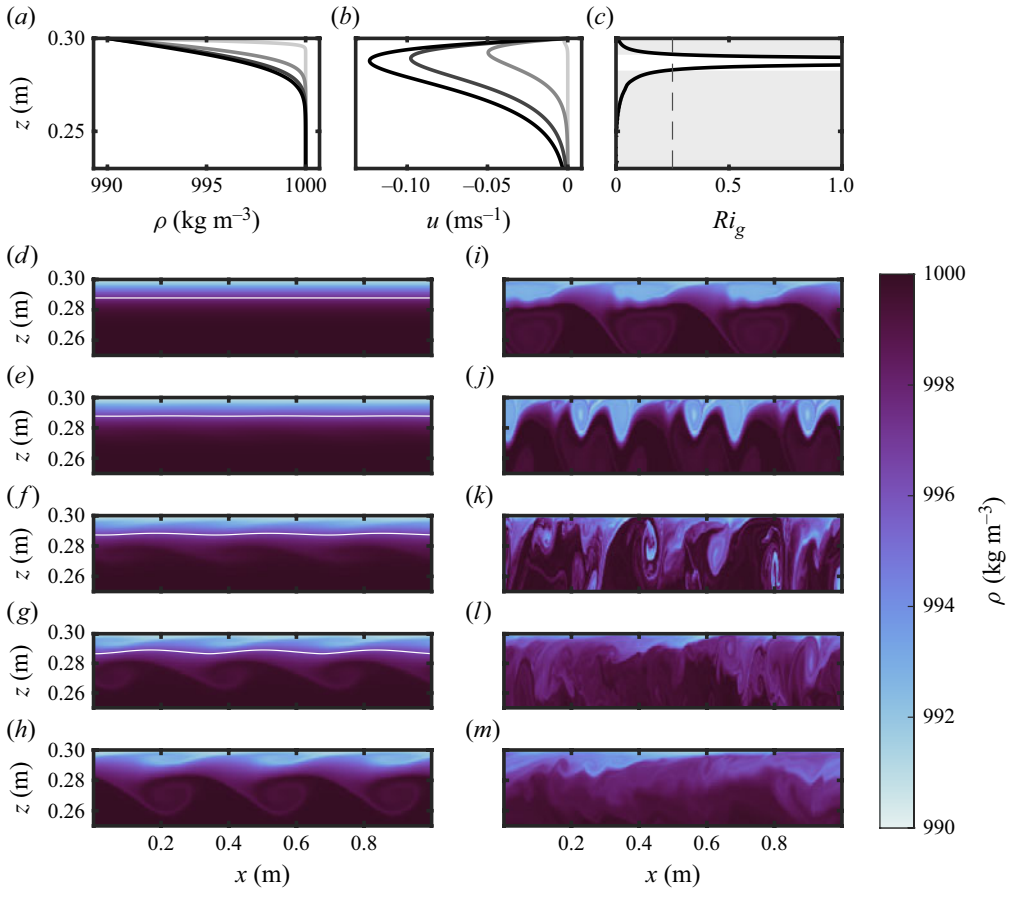


Figure 2. The evolution of flow in simulation ISO_Base. In (*a–c*) the evolution of profiles of (*a*) density, (*b*) streamwise velocity at $t = 5225$, 450 and 570 s and (*c*) profile of Richardson number at $t = 570$ s prior to instability forming, where shaded regions indicate depths where $Ri_g(z) < 0.25$. Panels (*d–m*) show the evolution of density fields at times $t = 400$, 570, 586, 594 and 600 s (*d–h*) prior to secondary instability, and $t = 610$, 630, 660, 690 and 770 s (*i–m*). In panels (*d–g*) the white line is provided as the isopycnal at the velocity maximum to aid visualisation of the internal wave. Supplementary material and movies are available at 1.

With this source of upslope buoyancy forcing, the flow begins to accelerate, forming a scythe shaped velocity profile (figure 2*b*). At the upper boundary, the velocity is 0 due to the no-slip condition, and similarly the ambient fluid is at rest owing to a lack of forcing at depth, in between the two is the velocity maximum. Between the upper boundary and the peak in velocity at $z \approx 0.29$ m, a strong shear layer ($\mathrm{d}u/\mathrm{d}z > 0$) forms, and between the ambient fluid and the velocity maximum, a further shear layer of the opposite polarity ($\mathrm{d}u/\mathrm{d}z < 0$) forms (figures 2*b*, 3*a*– and 3*b*). The flow is both laminar and parallel to the slope (and therefore also to isopycnals), and so drives no additional mixing (as confirmed by comparison of density profiles in a simulation with $\theta = 0$). During this phase (until $t \approx 570$ s) the flow is entirely one-dimensional (uniform in the streamwise direction) (figure 3*a*).

Following Carpenter *et al.* (2010*b*), it is useful to identify interfaces on which vorticity and gravity waves can propagate. The density profile indicates there is a single density interface that supports gravity waves that extends across the entire depth, however, gravity wave propagation will be concentrated over the region of stratification near the surface.

https://doi.org/10.1017/jfm.2026.11840 Published online by Cambridge University Press

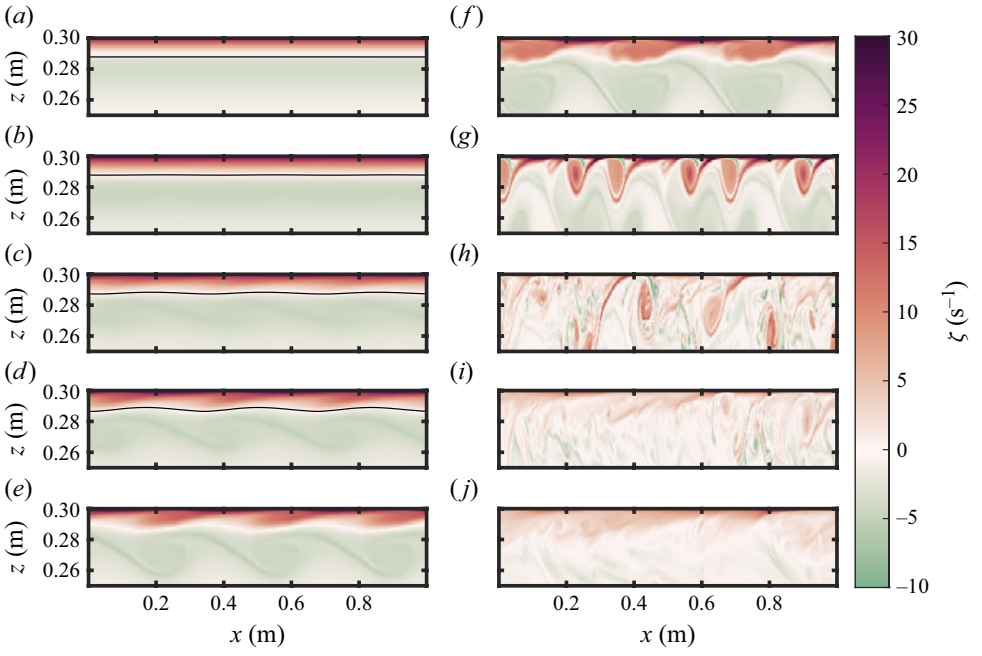


Figure 3. Time sequence of vorticity ($\zeta = \nabla \times \boldsymbol{u}$) outputs from simulation ISO_Base, where panels (*a–j*) match figure 2 panels (*d–m*) respectively.

The velocity profile indicates the presence of two vorticity interfaces (figure 2*b*), one approximately coincident with the density interface, and one just below it, with opposing signs.

Using the classical critical gradient Richardson number $Ri_g < 1/4$, we identify two regions of flow susceptible to shear instability from as early as $t = 70$ s. A near-surface region with $Ri_g < 1/4$ is driven by high shear at the no-slip boundary and a further deeper region where $Ri_g < 1/4$ from $z \approx 0.2725{-}0.285$ m occurs where the density gradient is gentle, and shear is moderate (figure 2*a–c*). These two regions are separated vertically by a stable region around the velocity maximum (where shear is therefore lowest and, at the velocity maximum itself, identically zero). However, despite the necessary, but not sufficient, critical Richardson number for shear instability being reached at this point, the flow remains stable. One dimensional mean flow profiles continue to dominate. Once the velocity structure has developed (by around $t = 70$ s) the flow always has regions where $Ri_g \ll 1$ and regions where $Ri_g \to \infty$, and hence $Ri_g < 0.25$ (or any other critical value) is a poor parameter for assessing stability of this flow.

3.2. *Primary instability of the base flow*

In numerical simulations, small perturbations on these interfaces grow into waves of finite amplitude on the interface (figures 2 *f* and 3*b*) propagating in the same direction as the main flow (right to left) at $-0.0859\ \mathrm{m\ s^{-1}}$ (slower than $U_{max} = -0.1263\ \mathrm{m\ s^{-1}}$) from $t \approx 580$ s. From the cusps of the waves, long wisping structures emerge in a paired system centred on the velocity maximum. On each resulting vorticity interface these wisping structures emerge, with smaller-amplitude wisps (geometrically constrained by the upper boundary) forming upward and clockwise, and larger-amplitude wisps that develop into overturning billows forming downward and anti-clockwise (figures 2*g*, 2*h*, 3 *d*, 3*e*).

https://doi.org/10.1017/jfm.2026.11840 Published online by Cambridge University Press

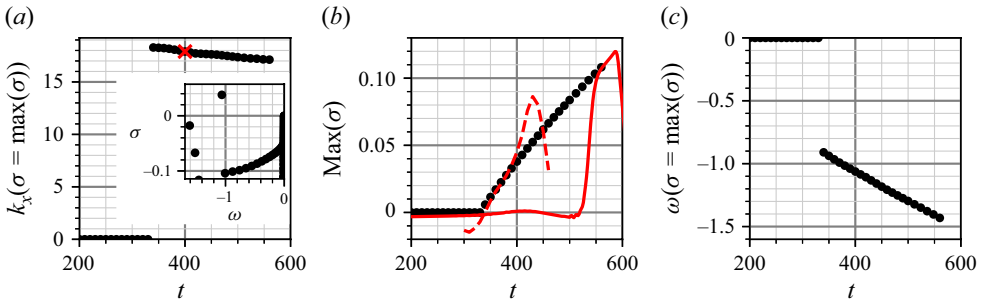


Figure 4. Time series of the wavenumber k_x (*a*), maximum growth rate $\max(\sigma)$ (*b*) and frequency ω (*c*) associated with the dominant mode emerging from vTG solutions (mode with the maximum growth rate) subject to simulation flow profiles. Panel (*a*) inset shows frequency growth rates associated with the k_x marked by the cross, demonstrating a single mode with $\sigma > 0$. Lines in panel (*b*) represent estimated growth rates of turbulent kinetic energy (TKE) for the simulation ISO_Base (solid), and the same simulation but initialised at $t = 300$ with the LSA dominant mode eigenfunctions (dashed).

3.2.1. *Linear stability of the time-evolving base flow*

To explain the instability, and the conditions required to go unstable, we first explore the time dependence of the dominant modes arising from solutions to the vTG system, subject to temporally evolving buoyancy and velocity background states. The time dependences of the dominant mode eigenvalue with $\max(\sigma)$ and its corresponding wavenumber $k_x(\sigma = \max(\sigma))$ and frequency $\omega(\sigma = \max(\sigma))$ are shown in figure 4. First, note that the LSA predicts a stable flow until $t \approx 340$ s, at which point a single dominant mode emerges with $\sigma > 0$, with σ growing approximately linearly with time beyond this point. Note that we do not perform computations after $t = 560$ s, at which point planar-averaged simulation profiles are dominated by the growing instability and LSA is no longer useful (see e.g. figures 2*e* and 2*f*). After $t = 340$ s, σ and ω change fairly linearly with time (σ increasing, ω decaying), while the dominant k_x slowly decreases with time, dropping from approximately 18 to 17 over 200 s. The inset of figure 4 (*a*) shows the single dominant mode with $\sigma > 0$, computed with profiles at $t = 400$ s with $k_x = 17.9$. This is indicative of all solutions for $340 \lesssim t \lesssim 560$ s. Note that the frequency ω of the dominant instability is negative, such that instabilities propagate in the direction of the mean flow.

To compare LSA solutions against simulations we have also estimated TKE growth rates following Howland, Taylor & Caulfield (2018). Instantaneous growth rates from simulation data are calculated as $\sigma_{sim} = (1/(2E))(\mathrm{d}E/\mathrm{d}t)$, where E is the perturbation kinetic energy calculated $(1/2)\langle(\boldsymbol{u}')^2\rangle$. Growth rates of ISO_Base are reported in figure 4(*b*) (solid red line). We see that unstable growth does not occur until $t \approx 520$ s for ISO_Base, but when the flow does go unstable the growth rates compare well against the LSA predictions, with $\sigma \approx 0.1$. The simulation TKE growth rate peaks at $t \approx 590$ s, at which point strong overturning dominates the dynamics (figures 2*f* and 2*g*). However, when the simulations are seeded with the appropriate perturbations, unstable growth occurs at the time predicted by the LSA (see figure 4*b*). Here, the simulation was restarted at $t = 300$ s with low-amplitude perturbations added to the flow profiles, taken from the eigenfunctions associated with the most unstable modes predicted by LSA (see Appendix B for details). In this case, the growth of E is consistent with LSA predictions until nonlinearity dominates ($t \gtrsim 400$ s), indicating that, while growth is possible during these earlier stages of flow development, it requires a particular form of perturbation to experience instability.

To develop our understanding of why the slowly evolving profiles go unstable at $t \approx 340$ s, we first revisit the planar-averaged simulation profiles, rescaling them by the

https://doi.org/10.1017/jfm.2026.11840 Published online by Cambridge University Press

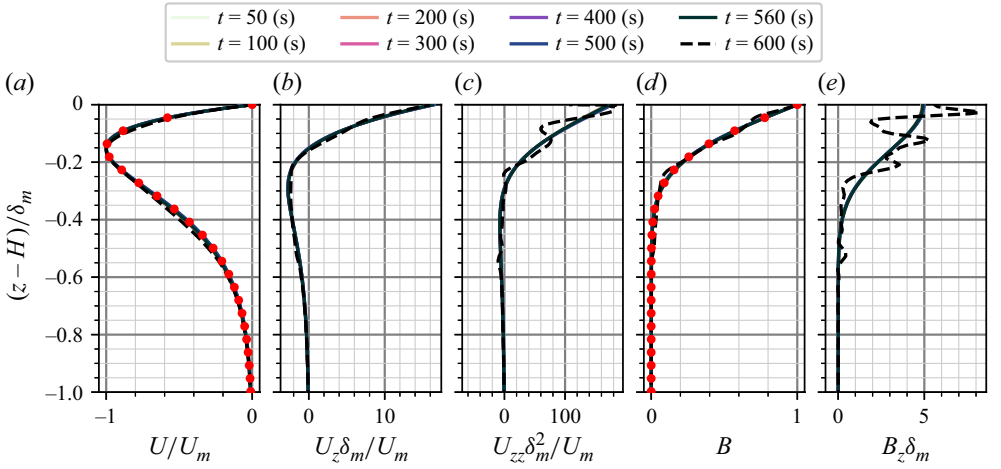


Figure 5. Time dependence of planar-averaged velocity, buoyancy and respective spatial derivatives, from simulation data, scaled by the absolute maximum velocity U_m and the boundary current thickness δ_m. Note that self-similar profiles from $t = 50$ to 560 s overlap and are hidden by the $t = 560$ s profile. The markers of panels (*a*) and (*d*) represent the analytical solutions for a convective flow developing on a vertically oriented heated plate (Ke *et al.* 2019).

time-varying maximum absolute velocity, U_m and the boundary current thickness, δ_m, which we define as the distance from the upper boundary down to the point beneath the velocity maximum where the absolute flow velocity reduces below 1 % of its maximum value. The planar-averaged time-varying simulation profiles of streamwise velocity, buoyancy and associated spatial derivatives, are reported in figure 5, where velocities are scaled by U_m and spatial coordinates by δ_m. When the vertical coordinate is taken as $(z - H)/\delta_m$, all appropriately scaled profiles collapse for $t \lesssim 560$ s, after which instabilities dominate the simulation (see e.g. the $t = 600$ s profile in figure 5). This clearly demonstrates that the flow is self-similar during its slow evolution phase, until instability dominates for $t \gtrsim 560$ s. Interestingly, δ_m appears to be an appropriate length scale to collapse the buoyancy fields, despite the comparatively thin density interface when compared with shear. This indicates that the ratio δ_b/δ_m is approximately constant over this time range (figure 7*d*), where δ_b represents the thickness of the buoyant jet, which we define as the distance from the upper boundary to the location where B is 1 % of its maximum value.

Figure 5 also includes the analytical solution for a temporally evolving convective boundary layer that develops on an isothermal vertically aligned plate (Illingworth 1950; Schetz & Eichhorn 1962; Ke *et al.* 2019). The present ice-sheet problem is equivalent to the convective boundary layer case if the wall were aligned with the gravity vector ($\theta = 90°$). Clearly, during initial flow evolution, flow development is identical between the two cases. The flows evolve due to diffusion from the wall, and through acceleration due to the streamwise buoyancy force (in the present case, $g_x = -g \sin\theta$). Until nonlinearity develops, it is unsurprising that both flows collapse to the same velocity and buoyancy profiles, subject to appropriate scaling.

It is informative to compare our LSA with that of Ke *et al.* (2019), who performed equivalent analysis on the vertically aligned heated plate. In figure 6 we present our solutions using the same scaling as figure 2 of Ke *et al.* (2019), which is based on the diffusive length and time scales

https://doi.org/10.1017/jfm.2026.11840 Published online by Cambridge University Press

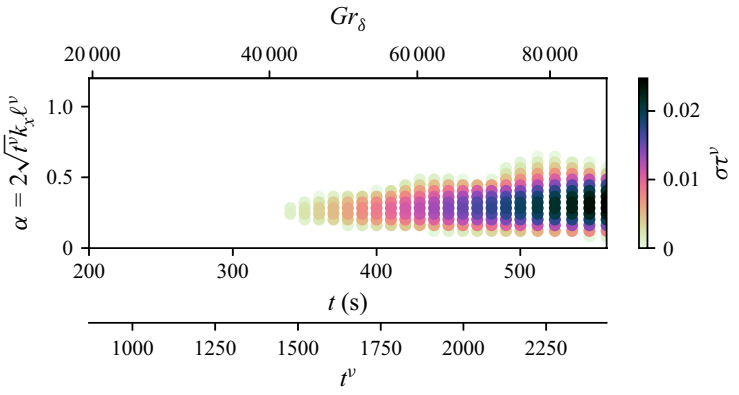


Figure 6. Linear stability of the temporally evolving stratified shear flow, presented with a diffusive scaling. Here, the wavenumber and growth rates are scaled by the diffusive length and time scales l^ν and τ^ν, and instability is presented as a function of dimensional time t, diffusive time t^ν and the Grashoff number Gr_δ.

$$\ell^\nu = \left(\kappa^2/g_r\right)^{1/3}, \quad \text{and,} \quad \tau^\nu = \left(\kappa/g_r^2\right)^{1/3}, \tag{3.1}$$

where g_r represents the reduced streamwise gravitational acceleration: $g_r = (\Delta\rho/\rho_0)g\sin\theta$. Definitions of the diffusive time $t^\nu = t/\tau^\nu$, wavenumber $\alpha = 2\sqrt{t^\nu}k_x\ell^\nu$ and growth rate $\sigma\tau^\nu$, are consistent with the definitions of Ke *et al.* (2019), where the wavenumber time dependence arises due to the time dependence of the base flow. Instability is also presented as a function of the time-dependent Grashoff number $Gr_\delta = g_r\delta_u^3/\nu^2$, where $\delta_u = \int_{-H}^{0}(U/U_m)\,\mathrm{d}z$ is the integral boundary layer thickness. As noted by Ke *et al.* (2019), the flow can be assumed to vary sufficiently slowly for LSA when the Grashoff number is large.

The present flow is unstable over a range of wavenumbers $\alpha \lesssim 0.6$, and for $t^\nu \gtrsim 1400$ or $Gr_\delta \gtrsim 40\,000$. This is considerably more stable than the vertically oriented flow of Ke *et al.* (2019), who observed instability for $\alpha \lesssim 2$, $t^\nu \gtrsim 50$ and $Gr_\delta \gtrsim 500$. Nevertheless, there are similarities between the linear stability of figure 6 and that of Ke *et al.* (2019), particularly the magnitudes of the growth rates and unstable wavenumbers, and the qualitative shape of the marginal stability curve. It is expected that, as the slope angle θ increases, the stability diagram would transition towards that of the vertically aligned problem of Ke *et al.* (2019).

This disagreement is of course due to the role of the vertical buoyancy force. We argue that the balance between vertical buoyancy forces and vertical shear (i.e. a Richardson number) controls the transition to instability. To this end, we reformulate the eigenvalue problem based upon time-invariant base profiles, with appropriate scaling by U_m and δ_m (figure 5). Time invariance of the base profiles further justifies our use of LSA to describe the dynamics for this temporally and spatially evolving flow. Rescaling the governing equations leads to the following system:

$$\frac{\partial \boldsymbol{u}^*}{\partial t^*} + \left(\boldsymbol{u}^* \cdot \boldsymbol{\nabla}^*\right)\boldsymbol{u}^* = -\boldsymbol{\nabla}^* p^* + b^* \boldsymbol{e}_g + \frac{1}{Re_u}\Delta^* \boldsymbol{u}^*, \tag{3.2}$$

$$\boldsymbol{\nabla}^* \cdot \boldsymbol{u}^* = 0, \tag{3.3}$$

and

$$\frac{\partial b^*}{\partial t^*} + \left(\boldsymbol{u}^* \cdot \boldsymbol{\nabla}^*\right) b^* = \frac{1}{Re_u Sc}\Delta^* b^*, \tag{3.4}$$

https://doi.org/10.1017/jfm.2026.11840 Published online by Cambridge University Press

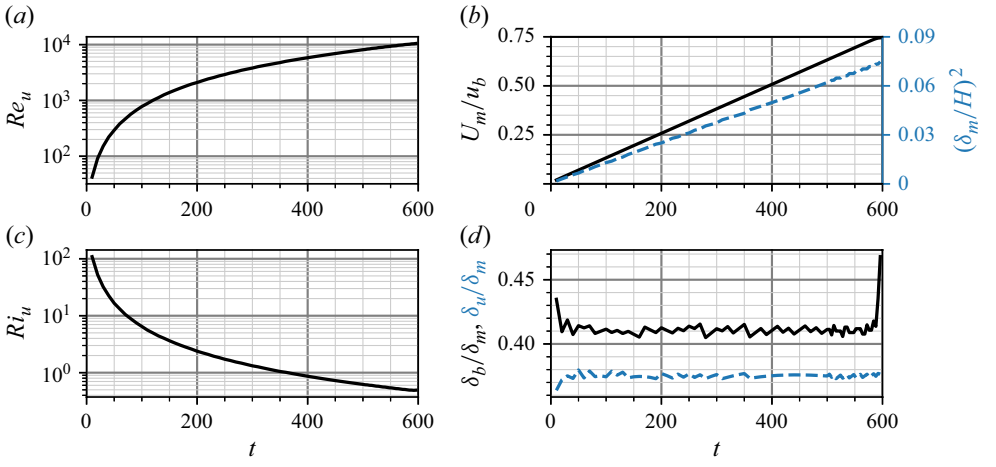


Figure 7. Time dependence of key dimensionless parameters obtained from planar-averaged simulation profiles.

where the $*$ superscript represents a dimensionless variable. Crucially, the buoyancy is now redefined as $b^* = Ri_u b$; the governing dimensionless parameters are therefore a Schmidt number, and time-varying Reynolds and Richardson numbers

$$Sc = \frac{\nu}{\kappa}, \quad Re_u = \frac{U_m \delta_m}{\nu} \quad \text{and} \quad Ri_u = \frac{\Delta\rho g \delta_m}{U_m^2} = \frac{\delta_m}{H}\frac{u_b^2}{U_m^2}, \tag{3.5}$$

where $u_b = \sqrt{\Delta\rho g H/\rho_0}$ and H is the domain depth. Flow evolution, and therefore transition to an unstable dynamics, is therefore controlled by the time dependence of Re_u and Ri_u rather than evolution of base flow profiles; likely either through a reduced ability of viscosity to mitigate shear instability through an increased Reynolds number, or through a reduced ability of buoyancy forces to suppress shearing, through a reduced Richardson number.

The time dependence of these parameters is reported in figure 7. First, note that the ratios δ_b/δ_m and δ_u/δ_m are approximately constant over the region of the time series where profiles are self-similar, fluctuating about values of $\delta_b/\delta_m = 0.41$ and $\delta_u/\delta_m = 0.375$. Secondly, note that both U_m/u_b and δ_m/H have a clear and trivial time dependence, with the velocity scale growing linearly with time and the boundary current width growing like the square root of time. As a result, we see that $Re_u \sim t^{3/2}$ and $Ri_u \sim t^{-3/2}$. The result of this is that both the Reynolds number and the Richardson number change by more than two orders of magnitude in the range $0 < t < 600$ s.

Figure 7 shows that, when instability develops at $t \approx 340$ s, Re_u has reached approximately 5000. More interestingly, $Ri_u \approx 1$ at $t \approx 340$ s, indicating that transition to instability occurs due to increased shear relative to suppressive buoyancy forces. To separate the influence of these two parameters we reformulate the vTG eigenvalue problem, instead assessing the linear stability of the rescaled time-invariant background state, $U^* = U/U_m$ and $B^* = Ri_u B$. While the values of Re_u and Ri_u arise naturally through flow evolution, here, we explore the wider parameter space to understand their role in instability. The resultant dimensionless eigenvalues and eigenvectors are denoted $\lambda^* = \sigma^* - i\omega^*$, $\hat{v}^*$ and $\hat{b}^*$ respectively. The growth-rate dependence of this rescaled system on Re_u and Ri_u is reported in figure 8(*a*), where the peak-finding algorithm has been adopted to find the maximum growth rate ($\max(\sigma^*)$) and associated scaled

https://doi.org/10.1017/jfm.2026.11840 Published online by Cambridge University Press

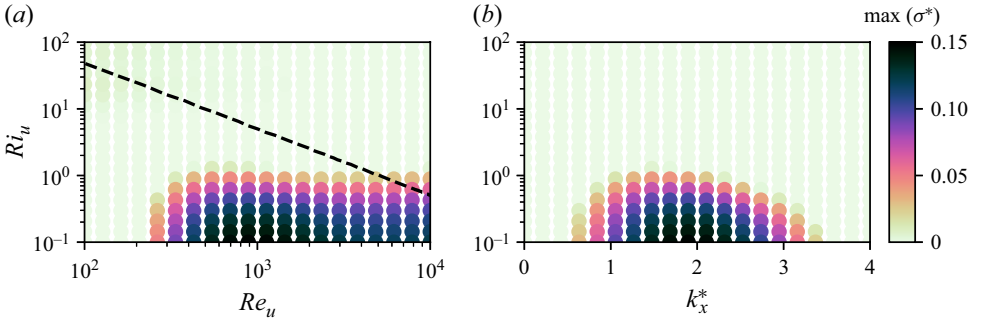


Figure 8. (*a*) Reynolds and Richardson number dependence of the maximum growth rate arising through the appropriately scaled vTG solutions, with parameters defined in (3.5). The dashed line represents parameter values arising through 2-D simulations. The maximum growth rates of panel (*a*) are obtained using the peak-finding algorithm. Panel (*b*) shows the wavenumber and Richardson number dependence of the maximum growth rate for $Re_u = 1000$.

wavenumber k_x^* for each of the marked points. The dashed line shows the parameter values that arise through simulations, combining data of figure 7. The unstable region of the phase space is bounded by $Re_u \gtrsim 250$ and $Ri_u \lesssim 1$. For $Re_u \gtrsim 1000$ the Reynolds number dependence is reasonably weak, although note that the flow is most unstable for $Re_u \approx 1000$, indicating that the mode is destabilised by viscosity, a behaviour similar to that of plane Poiseuille flow (Smyth & Carpenter 2019). There is a clear boundary between stable and unstable flow at $Ri_u \approx 1$, indicating that the balance between shearing and buoyancy forces plays a key role in the dynamics, with the maximum growth rate increasing with decreasing Ri_u. The region where the simulation crosses into the unstable regime is fairly insensitive to the Reynolds number, but highly sensitive to Ri_u. For most of the flow development the Reynolds number is high enough to enable unstable growth (figures 7 and 8), indicating that it is the crossing of the Ri_u threshold that finally enables flow transition.

For clarity the k_x^* dependence of the maximum growth rate is also reported in figure 8(*b*), where the Reynolds number is fixed to $Re_u = 1000$. This clearly shows a single peak in growth rate at $k_x^* \approx 1.8$.

The structure of the dominant mode is reasonably insensitive to Reynolds and Richardson numbers, so long as their values fall in the unstable regime. The mode is visualised in figure 9 for parameter values of $Re_u = 10\,000$, $Ri_u = 0.5$ and $k_x^* = 1.36$. Figure 9 also directly compares LSA eigenfunctions with simulation perturbations for case ISO_Base during the early stages of unstable growth at $t = 570$ s. There is clear strong agreement between the two datasets, providing further evidence that LSA is a valuable tool for assessing the primary instability of this flow. It is important to stress that (as with other figures) the vertical axes of figure 9 have been stretched to better visualise the strongly sheared modal structure near the upper surface. As a result, the lower vortical structures beneath the lower critical layer are more strongly affected by shear than presented in the figure. This is important when interpreting the nature of this instability.

These parameter values lead to an unstable mode with $\sigma^* = 0.074$ and $\omega^* = -0.94$, although we stress that the dominant modal structure is reasonably insensitive to parameter values so long as the mode is unstable. Critical levels are also shown, where the wavespeed of the mode matches the base flow speed, and indicate regions we may expect wave breaking. We see that these critical levels approximately denote the regions of strongest buoyancy and streamwise velocity perturbations. Vortical structures are most clear beneath

https://doi.org/10.1017/jfm.2026.11840 Published online by Cambridge University Press

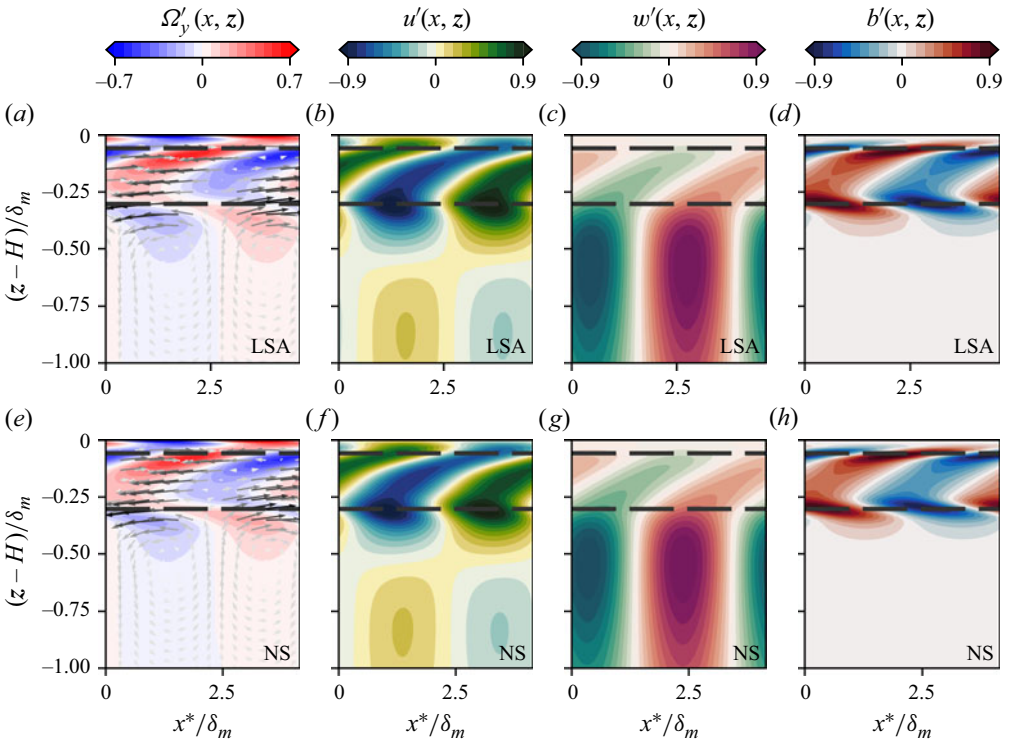


Figure 9. Visualisation of the dominant unstable mode, obtained through LSA, for $Re_u = 10\,000$, $Ri_u = 0.5$ and $k_x^* = 1.36$. Vorticity contours overlayed by arrows indicating flow direction, scaled and coloured by the velocity magnitude are shown in panel (*a*), while the streamwise and vertical velocity components are shown in panels (*b*) and (*c*). Panel (*d*) shows the buoyancy structure. Note that all quantities are scaled by respective maxima. The horizontal dashed lines represent critical levels where the wavespeed $c^* = \omega^*/k_x^* = U/U_m$. Modal structure is reported over one wavelength; note the stretched scaling of the y-axes to better visualise the strongly sheared near-wall structures. Numerical simulation data perturbations for case ISO_Base at $t = 570$ s, taken as instantaneous values with planar means subtracted, are reported in panels (*e–h*): spanwise vorticity (*e*), streamwise velocity (*f*), vertical velocity (*g*) and buoyancy (*h*). For reference, critical levels of LSA solutions overlay all simulation perturbations.

the critical levels which agree well with the 2-D simulation solutions where overturning is present (figure 2). However, the highest magnitude of velocity perturbations occurs in the region of highest mean velocity, bounded between the two critical levels with a peak at $(z - H)/\delta_m \approx -0.2$. The influence of shear is imprinted on the modes above the lowest critical level. Note also that the buoyancy and vertical velocity are out of phase.

3.2.2. *Sensitivity of instability to governing parameters*

To identify the ubiquity of these flow features to varying real-world conditions, a number of sensitivity simulations were carried out where the governing parameters (the slope, θ, and Reynolds number, $Re = u_b H/\nu$) were adjusted. Two methods of altering the Re were applied. Firstly, $\Delta\rho$ was doubled and halved, which in turn increases Re (via u_b) by factors $\sqrt{2}$ and $1/\sqrt{2}$, respectively. Secondly, ν was doubled and halved, with κ halved and doubled, respectively, such that the final governing parameter Sc is kept constant. Whilst the overall effect should be governed only by the overall result on Re, the two methods may give the reader better insight into the effect of differing boundary/far-field conditions (expressed via $\Delta\rho$), and scaling (expressed via ν).

https://doi.org/10.1017/jfm.2026.11840 Published online by Cambridge University Press

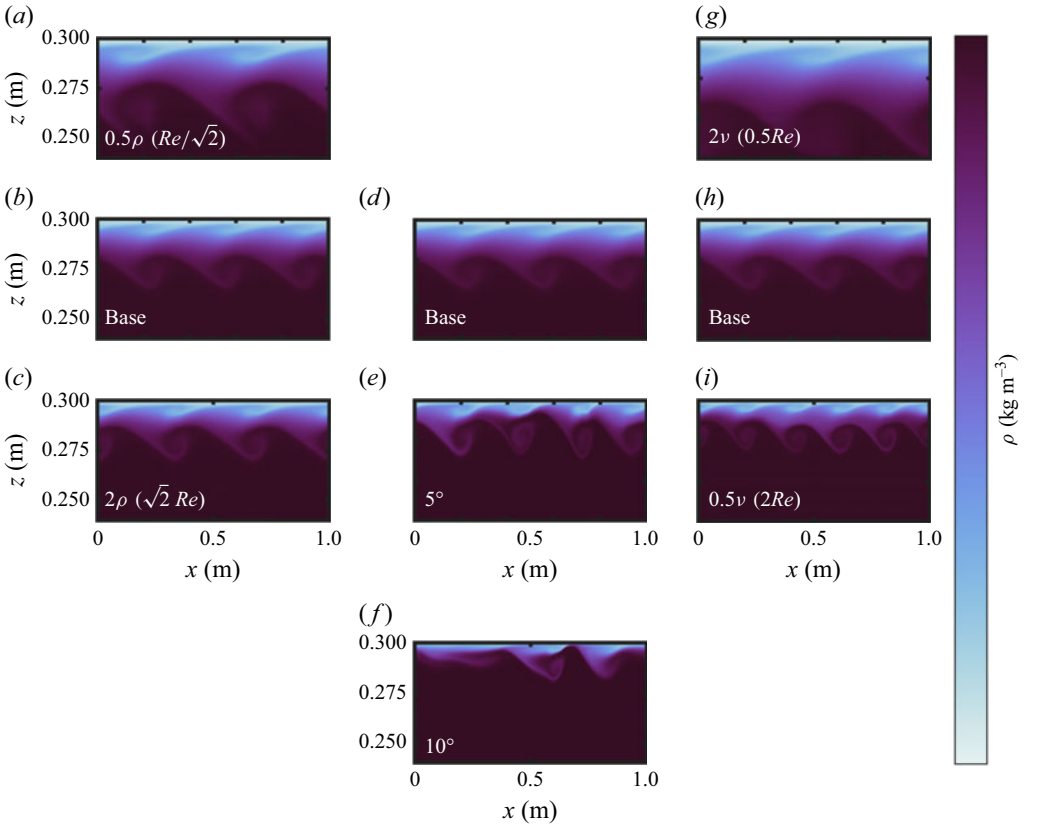


Figure 10. Single time outputs of density from simulations ISO_0.5x_rho at $t = 1030$ s (*a*, Supplementary material and movies are available at 2), ISO_Base at $t = 1030$ s (*b*,*d*,*h*), ISO_2x_rho at $t = 592$ s (*c*, Supplementary material and movies are available at 3), ISO_5_slope at $t = 370$ s (*e*, Supplementary material and movies are available at 4), ISO_10_slope at $t = 220s$ s (*f*, Supplementary material and movies are available at 5), ISO_2x_ν at $t = 835$ s (*g*, Supplementary material and movies are available at 6) and ISO_0.5x_ν at $t = 470$ s (*i*, Supplementary material and movies are available at 7).

Snapshots of the overturning billow structures are presented in figure 10. Overall, the flow characteristics are robust across the range of forcing slopes and density differences tested (figure 10). As density difference changes, in each case as the flow becomes unstable, the reflected wisping structure is reproduced. Reducing the density difference (and *Re*) (figure 10*a–c*), has the effect of allowing the density interface to develop over a longer time before going unstable, and therefore the density interface becomes thicker before instability begins. Overall, the effect on billow size (both in amplitude and wavelength) is to decrease as the density difference increases. Similarly, the effect of increasing viscosity (and therefore *Re*) also results in smaller (amplitude and wavelength) billows forming at earlier times at higher Reynolds numbers. A rough estimate of the relevant field-scale Reynolds number, assuming that flow speeds remain at approximately the same scale (Jenkins 1991), with $H = 100-1000$ m, and ν the same as in ISO_Base, giving $Re = 10^7-10^8$. Although it is impossible to extrapolate the relatively small changes in *Re* explored here to these much higher values, it is reasonable to assume the vertical extent of the instabilities (as a proportion of total depth) would continue to decrease, with more rapid cycles of instability and re-stability.

https://doi.org/10.1017/jfm.2026.11840 Published online by Cambridge University Press

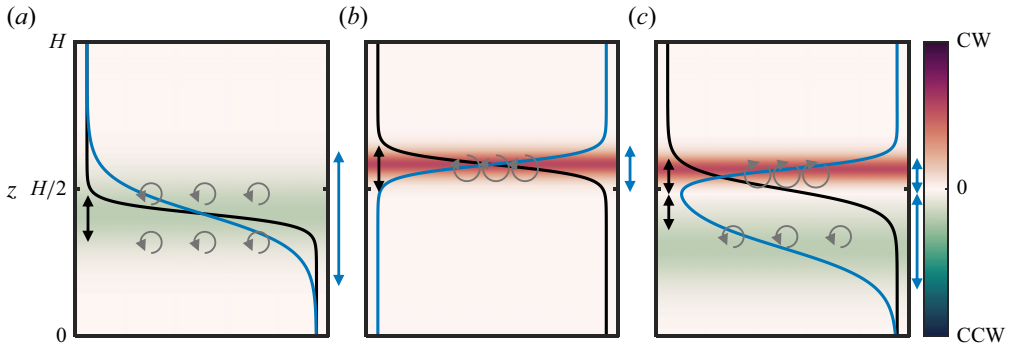


Figure 11. Schematic representation of profiles producing the canonical Holmboe (*a*), KHI (*b*) and the paired instability presented here (*c*), with horizontal velocity profile in blue, density profile in black, and a sense of the vorticity in the background colours (marked with clockwise, CW, and counter-clockwise, CCW). Circular arrows indicate the effect of the vorticity on shear interfaces, and the relative depths of shear and density interfaces are marked via the vertical arrows in blue and black for velocity and density respectively for each panel.

Changing slope steepness has a similar effect, although the relative contributions of changing gravity forcing on u and w becomes evident by the 10 ° simulation. Fundamentally the same instability is produced for the steeper slopes of 5° and 10° (figure 10*d–f*), and as with increasing the density difference, increasing the slope reduces billow dimensions, but additionally also produces more deformed billows (figure 10*f*). As the gravitational vector strays considerably from vertical, the system switches from one where density is able to stabilise the flow at small slopes, to one where density is destabilising and tending to overturning at steep slopes. Since these regimes with steeper slopes have been studied elsewhere (e.g. Carey & Gebhart 1981; Cenedese & Gatto 2016; McConnochie & Kerr 2018), here, we focus only on shallower slopes, and note that slopes beyond 5° show a transition towards the convection-driven instability regime (Ke *et al.* 2019).

3.2.3. *Mechanisms of the shear instability*

The stratified shear instability described above is unusual compared with the canonical instabilities described throughout most of the literature (figures 11*a* and 11*b*). Key to understanding the instability is the opposing directions of shear above and below $z(u = U_{max})$, with a stabilising density gradient throughout that velocity structure. This results in the sense of rotation of vortices each side of the velocity maximum being in opposing directions. Two interacting modes of instability are observed each side of the velocity maximum, and unlike canonical versions of mode interactions, these modes are both propagating in the same direction, due to the opposing directions of shear (figure 11*c*). The wave resonance interpretation of instability precludes the instability of certain jet-like channel flows such as these (Smyth & Carpenter 2019), but as shown in Appendix C, the flows are able to go unstable where the jet is bounded by fluid with constant (including 0) velocity.

A further complicating factor is the presence of a solid upper boundary which directly intersects both shear and density interfaces. Given these complications, identifying the forms of these modes against descriptions and definitions based on idealised flows is difficult. Whilst a full diagnosis is beyond the scope of this study (and may not yield

https://doi.org/10.1017/jfm.2026.11840 Published online by Cambridge University Press

additional insight into the useful dynamics of the flow), some considerations to these definitions are considered here.

Invoking descriptions based on the form of the instability itself, rather than based on profile-based measures, Parker, Caulfield & Kerswell (2020) define KHI as shear instability involving overturning of the shear layer, whereas HWI involves propagating vortices either side of the shear layer. For the instability below the velocity maximum, vortices indeed form below the shear layer, indicating that instability is a HWI-type instability. For the instability above the velocity maximum, the shear continues throughout the layer, perhaps suggesting that the only available mode in this region is KHI indicating overturning of the shear layer itself.

Other work has used the ratio, R_i, of velocity variation length scale ($h_{u,i}$) to density variation length scale ($h_{\rho,i}$), as a diagnostic for Holmboe instability, specifically where $R > 2$ indicates HWI is present (Alexakis 2007; Carpenter *et al.* 2010*b*). Split into each instability structure by the velocity maximum, the upper shear layer ($i = 1$) $h_{u,1} = h_{\rho,1} = H - z(u = U_{max})$, by definition returns $R_1 = 1$, whilst for the lower shear interface ($i = 2$), $h_{u,2} = \delta_u - h_{u,1}$ and $h_{\rho,2} = \delta_\rho - h_{\rho,1}$, giving $R_2 = 3.27$. Again, this criterion indicates mixed instability types, with KHI at the upper interface, and HWI on the lower layer.

Finally, we consider a descriptive diagnostic based on the eigenfunctions of dominant modes (see figure 9, and Zhu *et al.* (2024, figure 5). In figure 9, the modal structures beneath the velocity maximum show characteristics of the HWI, specifically two pairs of counter-rotating roll cells, centred at the lower critical level, whilst above the velocity maximum, alternating (strongly sheared) bands dominate the structure in both vorticity and density (figures 9*a,* 9*e,* 9*d* and 9*h*).

Application of the wave interaction-based diagnostic from Carpenter *et al.* (2010*a*) may provide further details as to the modes of instability. However, despite remaining uncertainty as to the mode of the upper instability, this work identifies complex systems of interacting modes of primary stratified shear instabilities. Paired interactions affect the leading-order behaviours of the secondary instability, and subsequent turbulent mixing with the dynamics playing out differently to two unpaired stratified Couette flows at the point of secondary instability due to this pairing between vorticity interfaces.

3.3. *Secondary instability of the flow and the transition to turbulence*

3.3.1. *Secondary instability and long-term evolution in two dimensions*

Once billows begin to overturn, the dynamics can only be represented by time-evolving nonlinear simulations, so we return to qualitative descriptions of 2-D SPINS simulations in order to test the mechanisms by which the flow may undergo cyclic or marginal instability equivalent to those proposed by Smyth, Nash & Moum (2019). Here, we define the system as undergoing cyclic instability if: (*a*) there is a cycle of instability, turbulent growth, turbulent decay and forcing towards instability, (*b*) multiple cycles of instability that occur in the same manner, indicated here by self-similarity of profiles during the forcing stage, meeting Re_u and Ri_u thresholds at instability, and similarity of the unstable mode.

As the overturning pattern develops, further shorter waves develop on the interface between the counter-rotating wisps/billow (figures 2*h,* 3*i* and 3 *e,* 3*f*). Specifically, as these secondary waves form, the anticlockwise vorticity of the lower layer drives shedding of parcels of upper layer fluid downwards (across the leading edge of the lower billow) (figures 2*j–l*, 3*g–i*). Secondary instability appears to form from these secondary waves – smaller-scale billowing structures, that drive the true degeneration into a state where turbulent mixing is active (figures 2*k–l* and 3*h–i*).

https://doi.org/10.1017/jfm.2026.11840 Published online by Cambridge University Press

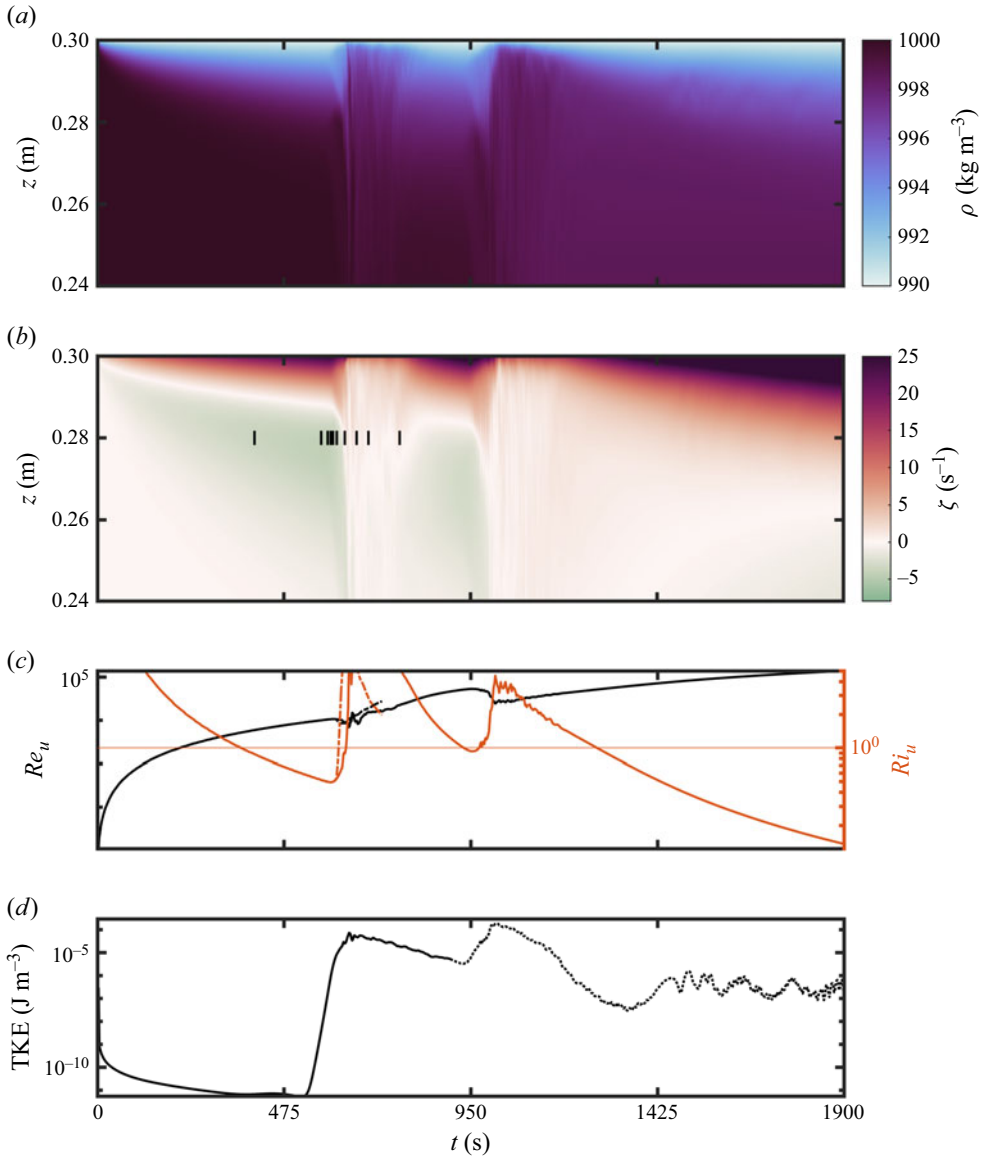


Figure 12. The long-term evolution of ISO_Base, showing Hovmöller plots of density (*a*), and vorticity (*b*) as well as evolution of Re_u and Ri_u (*c*). Hovmöller plots are each taken for a vertical profile at the mid-point of the domain. Lines in *b* indicate timings of panels shown in figures 2 and 3, the reference line in (*c*) shows $Ri_u = 1$, with two dimensions (solid line) and three dimensions (dashed line) shown. Panel (*d*) shows evolution of TKE for ISO_Base simulation over the initial cycle of instability (solid line) and subsequent evolution (dotted line).

The first criterion appears to be met for at least these two cycles (figures 12*a* and 12*b*). Once turbulence has been produced from the secondary instability, turbulent diffusion (mixing at the small scales) smooths shear and buoyancy gradients, so that the production of turbulence by the transfer of kinetic energy from the mean flow decreases and dissipation dominates (figures 2*m*, 3*j* and 12*b*, 12*d*). This decaying of turbulence over around 150–200 s allows the buoyancy forcing at the upper boundary to re-stratify the fluid, producing renewed forcing for the mean flow to grow. Over time, the re-stratifying

https://doi.org/10.1017/jfm.2026.11840 Published online by Cambridge University Press

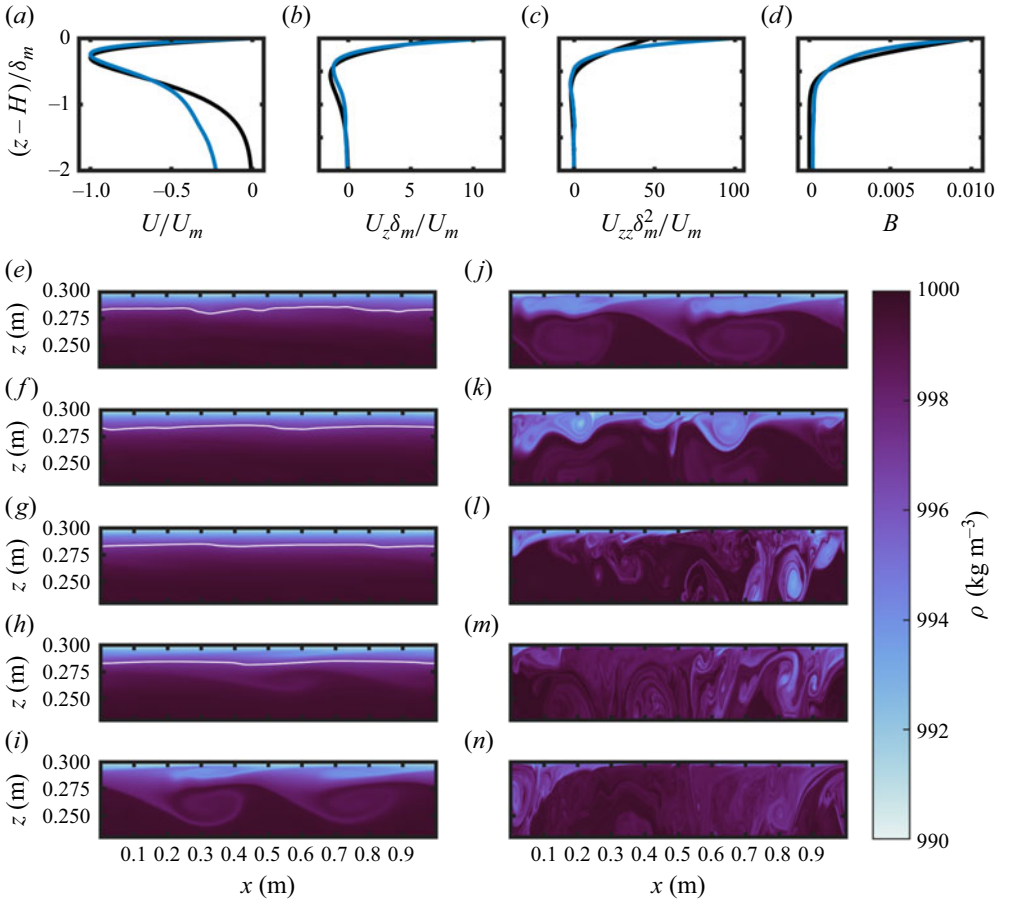


Figure 13. As in figure 2, but for the second instance of the instability forming. (*a–d*) show scaled forms of the respective profiles at times $t = 570$ s (black) and $t = 894$ s (blue) for assessment of self-similarity in later iterations. Panels *e-n* show times $t = 850$, 894, 914, 934, 954, 966, 994, 1014 and 1054 s respectively.

density boundary condition maintains a strong top to bottom density difference, and the fluid re-forms to a stratified boundary current state resembling earlier times (figure 13*a–e*). The flow develops to instability once again (figure 13 *f-i*) in a very similar manner to that described in §§ 3.2 and 3.3. Throughout this second cycle of instability, profiles are broadly self-similar and meet similar criteria of Re_u and Ri_u (figure 12*c*), and meet the second criteria for cyclic instability.

Over time, this 2-D mixing process is an efficient means of vertical mixing, and the pycnocline thickens substantially, exerting an upslope buoyant forcing throughout the water column. A more diffuse lower shear region forms after the second cycle of this instability after $t \approx 1200$ s (figure 12*a*). Once this dynamics begins to be affected by the lower boundary, the stability criteria Ri_u and Re_u based on δ_u is no longer applicable, since δ_u is now bounded by the lower boundary. It is possible that cyclic behaviour could continue beyond this time if the vertical extent of the domain were longer, but in these simulations, the instabilities stop due to constraint of the flow by the lower boundary, and the dynamics deviate from the geophysically relevant problem.

https://doi.org/10.1017/jfm.2026.11840 Published online by Cambridge University Press

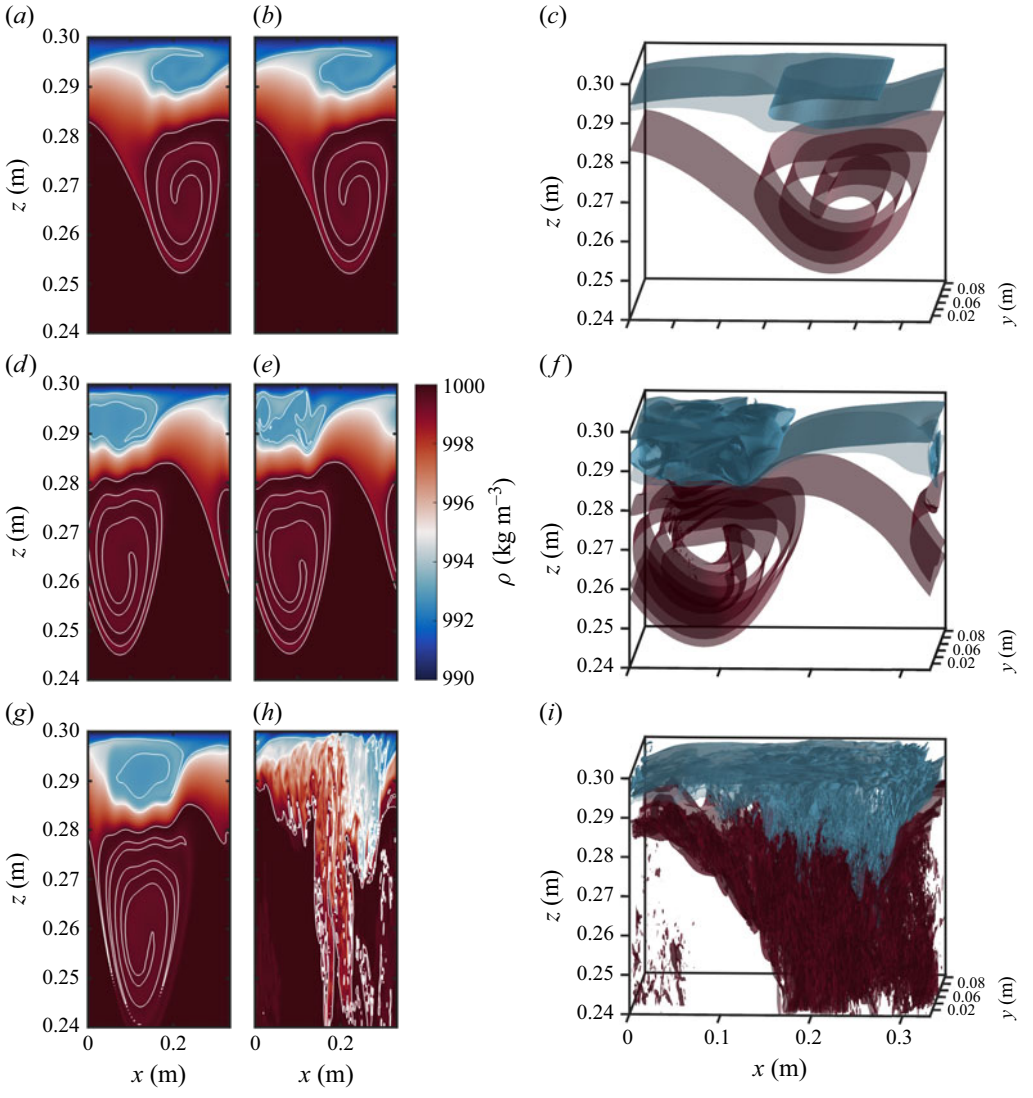


Figure 14. Early 3-D evolution of the secondary instability (centre, right) compared with the 2-D simulation ISO_Base at the same time (*a*,*d*,*g*). Shown for a $x-z$ slice for density (*b*,*e*,*h*) where contours representing the density isosurfaces shown in *c*,*f* and *i* are added in white. Top panels show $t = 604$ s middle panels show $t = 610$ s and lower panels show $t = 618$ s. Note z axis exaggerated from previous figures.

3.3.2. *Secondary instability and long-term evolution in three dimensions*

To test the effects of spanwise variability on the instability, a 3-D extension simulation of ISO_Base was conducted. The outputs of ISO_Base at $t = 570$ s, just prior to the primary instability forming, were extended into the spanwise direction, where $L_y = 0.128$ m, and $N_y = 128$, with white noise added in the spanwise direction to velocity fields to trigger any instabilities (in the same manner as at initialisation for 2-D simulations). In addition, the x domain was reduced by one billow wavelength, so that $L = 0.66$ m and $N_x = 684$, to optimise the computational efficiency. The evolution of the primary instability was confirmed to occur without significant spanwise variability or 3-D effects (figure 14*a–c*), so 2-D simulations are sufficient until this stage. Spanwise variability only

https://doi.org/10.1017/jfm.2026.11840 Published online by Cambridge University Press

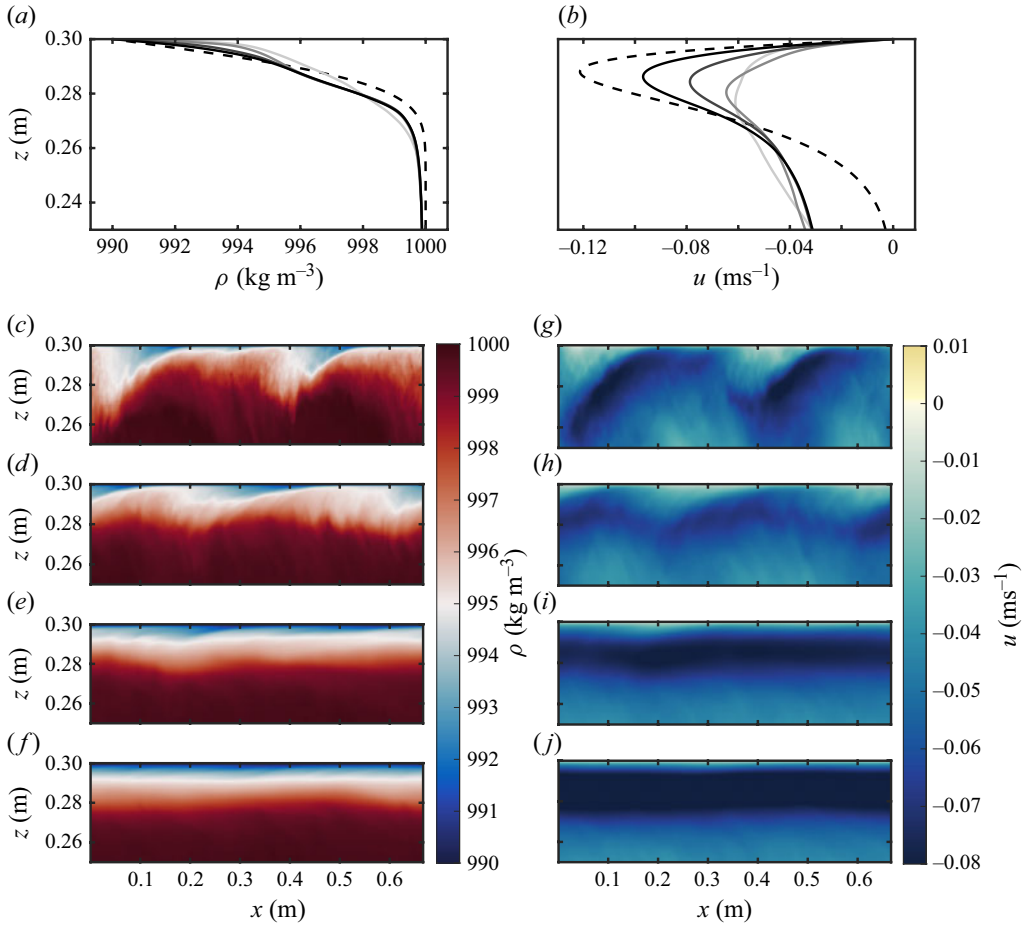


Figure 15. Late 3-D evolution of the secondary instability. Shown for a $x-z$ slice for density (*c–f*) and horizontal velocity (*g–j*). Corresponding profiles of horizontally averaged density (*a*) and along-slope velocity (*b*) are shown. Panels (*c–f*) and (*g–j*) and the profiles in increasing darkness are at times $t = 625$, 645, 655 and 688 s respectively. Dashed lines in (*a*, *b*) show reference profiles from $t = 560$ s (as in figure 5).

emerges once the upper and lower billows are significantly overturning and the flow is undergoing secondary instability, at which point the 2-D and 3-D simulations rapidly diverge (figures 14*d* and 14*e*). In contrast to the continued overturning and formation of waves on the interface between the billows observed in 2-D simulations (figure 14*d*), in 3-D simulations, the billows themselves undergo a transition towards a turbulent state (figures 14*e,* 14*f,* 14*h* and 14*i*), in line with theory on 3-D overturning. Small scale structures emerge, but unlike in the 2-D case, these are not cast downwards into the ambient fluid, instead the turbulence decays over a relatively rapid time scale (figure 15*e*).

It is important to note that these 3-D simulations do not include a Coriolis acceleration term which would deflect the base flow (to the form shown by e.g. Jenkins 2021) and likely result in more 3-D instabilities than those shown here. The more realistic mixing processes in 3-D simulations over a single cycle of instability result in a broadly similar process to their 2-D equivalents studied here. However, the improved representation of turbulent dissipation and mixing means the pycnocline does not thicken in the same manner, and shear remains constrained to the upper part of the water column (figure 15*b*). Whilst it

https://doi.org/10.1017/jfm.2026.11840 Published online by Cambridge University Press

remains unclear how well the similarity of the instability is maintained through subsequent cycles of instability from just a single cycle of instability, this indication of suppressed long-term deepening of the pycnocline indicates cyclic instability is more likely to occur when the 3-D dynamics is considered.

4. Discussion

This flow with a re-stabilising buoyancy flux across a tilted interface, which produces a unique dynamics, is likely to be a key feature of geophysical settings where a stable boundary layer forms over surface topography, but possibly unique in the ocean to the sub-ice-shelf environment and highly influential in driving mixing of temperature and salinity. Similar flows exist in the idealised form of stratified plane Poiseuille flows (e.g. Lloyd *et al.* 2022; Lloyd & Dorrell 2024), and turbulent gravity currents in a channel (e.g. Cantero *et al.* 2009). Consideration of gravity currents by Wells, Cenedese & Caulfield (2010) discusses the two sources of turbulence in density currents as interfacial entrainment at the boundary between the different density layers (expressed in plume-type models as the entrainment ratio, E) and drag at the solid lower boundary (expressed through the drag coefficient, C_d). In the flows considered in this paper, it is clear that the hard cutoff with the no-slip upper boundary generates a shear layer that is interacting with the generation of turbulence and shear at the diffuse boundary to the ambient fluid, whilst the continuous gradient of density throughout a significant portion of these two shear layers produces different dynamics to that observed in the earlier studies. The combination of continuous and multiple interfaces along with interactions of the flow with solid boundaries (Holt 1998; Baglaenko 2016; Liu, Kaminski & Smyth 2023) impact these instabilities, and as is shown in this paper, drive a new dynamics.

Whilst laboratory experiments and direct numerical simulations have been carried out for similar ice–ocean boundaries with steeply tilting ice (e.g. Kerr & McConnochie 2015; Gayen, Griffiths & Kerr 2016; McConnochie & Kerr 2018; Mondal *et al.* 2019) (see recent review from McCutchan & Johnson (2022)), studies for gently sloping ice surfaces are restricted to LES (e.g. Vreugdenhil & Taylor 2019; Begeman *et al.* 2022; Anselin *et al.* 2024) which, due to underlying assumptions in the sub-grid-scale model, may not resolve this new shear dynamics. Across various approaches, the general form of vertical profiles of density and streamwise velocity are consistent (Jenkins 2016; Mondal *et al.* 2019; Begeman *et al.* 2022; Patmore *et al.* 2023), indicating the key research question is what the routes to mixing and turbulence are in such flows.

In this case, evolution of these mixing events is considerably different to those observed in the canonical shear instabilities of Holmboe or Kelvin–Helmholtz. The initial instability is Holmboe-like, with a continual scouring of the pycnocline, rather than complete overturning of the pycnocline (due to separation of buoyancy and vorticity interfaces). This supports the theory of continuous marginal instability, which cannot be sustained for vertical wall systems (Ke *et al.* 2023). However, in contrast with those earlier results, later development of the flow becomes more vigorous, and almost analogous to later stages of KHI-like instability, with a complete decay to a turbulent state (although via a different mechanism).

Previous work using 1-D analytic models incorporating rotation has identified a marginally stable state of the pycnocline (Jenkins 2021; Anselin *et al.* 2024) under-ice shelves, a feature that may be ubiquitous in geophysical settings (Salehipour, Peltier & Caulfield 2018; Smyth & Carpenter 2019). The criterion for this marginal stability for the ice-shelf–ocean boundary remains an open question, with deviation around a critical Ri_g gradient through the pycnocline suggested by Jenkins (2021), whilst Anselin *et al.* (2024)

https://doi.org/10.1017/jfm.2026.11840 Published online by Cambridge University Press

instead found the boundary current was governed by a critical shear (itself dependent on basal slope), without the same dependence on buoyancy gradients. Here, our analysis of the linear stability of profiles identifies the instability of these profiles is dependent on both Re_u and Ri_u. If the system over longer time scales is assumed to deviate around the point of instability, this analysis may point towards the interplay of a combination of the shear and buoyancy gradients.

The instability of the flow is found to be poorly predicted by $Ri_g < 1/4$, instead LSA of the relevant profiles reveal patterns of instability based on Re_u and Ri_u. In particular, a region with $Ri_g \ll 1/4$ will exist from very early in the simulation (once shear begins to develop) due to the thick shear layer compared with the buoyancy (controlled through Sc), whilst a region with $Ri_g \gg 1/4$ will also exist at the velocity maximum (where shear is zero). The use of LSA enables the identification of such regimes, whilst its use is validated both by excellent agreement between vertical structures (figure 9) and growth rates (figure 4). The validity of LSA is confirmed by the self-similarity of profiles during the flow evolution, and the relative insensitivity of the structure of the dominant mode to Reynolds and Richardson numbers, meaning the flow profiles are effectively steady state, with a time dependence felt through Re_u and Ri_u.

Salehipour *et al.* (2018) argue that marginal instability in strongly stratified flows is more likely linked to the continuous, 'slow burn' features of HWIs, than the episodic 'flaring' KHIs. Subsequent work calls into question the exact mechanisms by which marginal instability can be achieved for stratified shear (Zhou 2022; Stastna *et al.* 2025). These simulations identify further mechanisms by which a marginally stable state might be achieved, via a combination of slower, more continuous scouring in the primary instability, followed by episodic overturning mixing in the secondary instability. We show evidence of cyclic instability where energetic turbulence diffuses away the sharp velocity gradients thus increasing Ri_u, and re-starting the cycle. It is important to note that periodic simulations may be more susceptible to cyclic behaviour than large domains relevant to geophysical settings (Smith, Caulfield & Taylor 2021; Vieweg & Caulfield 2026), and further work is required to understand the sensitivity of mechanisms for cyclic behaviour presented here.

Now the fundamental dynamics is understood in the simplest case, future work is needed to identify the role of various processes present in the real world ice shelves. Firstly to consider the sensitivity of simulations to varying Sc from the $Sc = 7$ used here for computational efficiency to higher Sc representative of salt, the main stratifying agent under-ice shelves. Only when two properties (temperature and salinity) with widely differing diffusivities are considered can simulations include the effects of double diffusion, which can be a significant factor in ice-shelf melting regimes under particularly quiescent conditions (Middleton *et al.* 2021, 2022; Rosevear *et al.* 2021, 2022), in turn defining the profiles of buoyancy forcing. Furthermore, planetary rotation exerts a strong control over the development of the shear profile. Rotation of the velocity vector leads to non-zero shear at the speed maximum, and is therefore likely to produce truly 3-D instabilities that are not represented by simulations herein. Meanwhile viscous effects are limited to the Ekman layer, beyond which the flow is close to thermal wind balance. Incorporating such effects would be critical to compare simulations analogous to these with past LES studies.

5. Conclusions

In this paper, we identify a complex paired instability that emerges and drives the transition to turbulent mixing under-ice shelves using high-fidelity numerical simulations. This flow

https://doi.org/10.1017/jfm.2026.11840 Published online by Cambridge University Press

exhibits features of both the slowly evolving HWI, with scouring-based mixing typically associated with marginally stable flows; and of the flaring KHI associated with short lived, but vigorous overturning-based mixing. Such features emerge after a long phase of slowly evolving, diffusion-based flow, and are well predicted by LSA of profiles, with the onset of instability predicted by a combination of Ri_u and Re_u, rather than $Ri_g < 0.25$ used for many other stratified shear flows. Cyclic behaviour in the instabilities forming, mixing by turbulence, decay of turbulence, and then flow building back to instability is evidenced in 2-D simulations by changes in Ri_u (figure 12); instabilities develop for $Ri_u < 1$ which reduce shear and increase Ri_u above 1, where turbulence decays and flow begins to sharpen again.

As the flow evolves, increasing levels of complexity are required in the modelling approach. The early evolution of the flow is entirely one-dimensional, and the initial instability is well predicted by LSA. That analysis provides valuable insight into the regimes of instability, and the mechanisms driving instability, but the flow rapidly evolves outside the range of validity for small-amplitude perturbations, at which point time-resolved numerical simulations in two dimensions are required. Such simulations are effective at simulating the initial transition from a 1-D to 2-D state under the primary instability, but once overturning has occurred, 3-D secondary instabilities form, requiring 3-D simulations. Such a combined approach of LSA of 1-D profiles, 2-D simulations and extensions of these into the third dimension provide a valuable combination of insights into the behaviour of these flows. Building on the approach in this manuscript, further valuable insights into these systems could be identified via a LSA generalised to any slope angle (from the near-horizontal slopes in this study, to the vertical walls of Ke *et al.* (2019)) following the approach of Atoufi *et al.* (2023). Additionally, work to implement a sorting-based method similar to Winters *et al.* (1995) for these periodic, tilted domains with surface forcing could yield interesting insights.

The key research question underpinning any investigation into the ice-shelf–ocean boundary is to understand better the rates at which oceanic heat can be mixed towards the ice and lead to melting, a pre-cursor to which includes improving the resolution towards full turbulence-resolving simulations. Further work is required to identify the applicability of existing parameterisations to flows with these paired instability features, but given the difficulties observing such features *in situ*, this work presents an important step towards understanding the mechanisms and regimes and of shear-driven mixing at this interface.

Supplementary movies. Supplementary movies are available at https://doi.org/10.1017/jfm.2026.11840.

Acknowledgements. We thank C. Subich, A. Grace and M. Stastna for their contributions to developing this case in SPINS. This work used Northumbria University's Oswald High-Performance Computer.

Funding. CJL was supported by an Early Career Fellowship funded by The Leverhulme Trust.

Declaration of interests. The authors report no conflict of interest.

Data availability statement. The data that support the findings of this study is openly available at Northumbria University's data repository, accessible at https://doi.org/10.25398/rd.northumbria.c.7941254.

Author contributions. All authors contributed to development of the project, review and editing the manuscript. AJ and SGHE were responsible for project conceptualisation, SGHE developed, carried out, analysed and visualised the numerical simulations and wrote the original draft of the manuscript. CJL conducted the LSA and prepared the figures and initial draft for this section.

https://doi.org/10.1017/jfm.2026.11840 Published online by Cambridge University Press

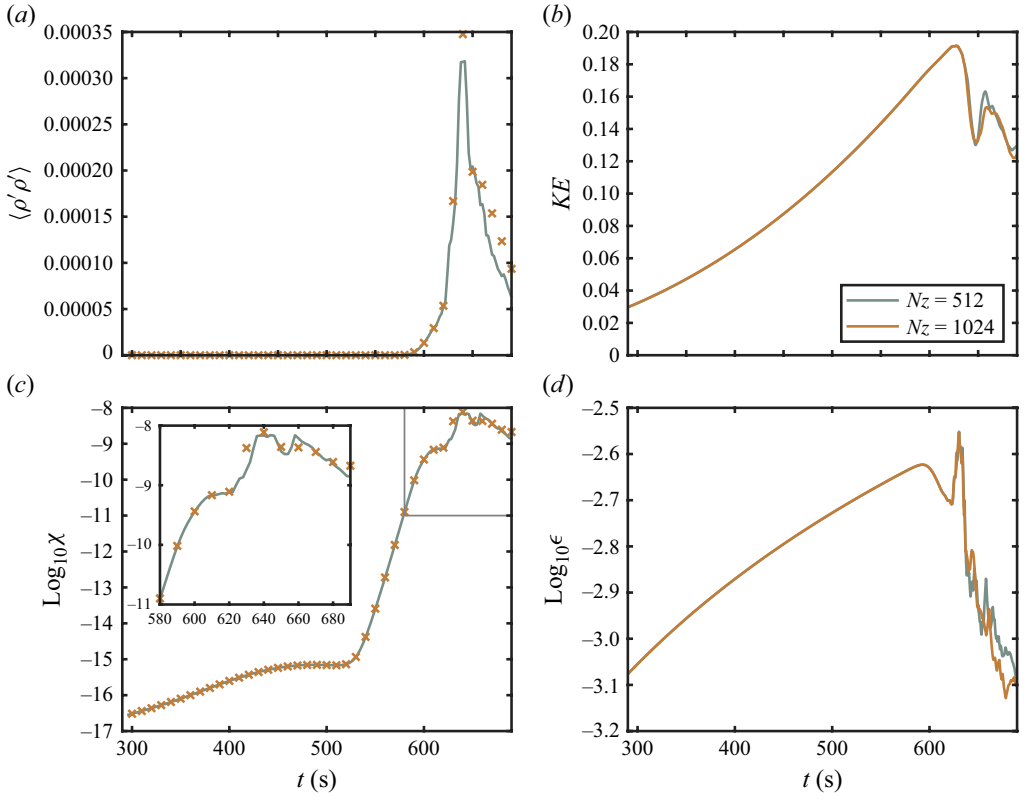


Figure 16. Grid sensitivity of simulation ISO_Base shown with the domain-integrated density variance (*a*), density variance dissipation rate (*b*), KE (*c*) and dissipation rate (*d*) for the 400 s sensitivity simulation for sensitivity simulations with $Nz = 512$ and $Nz = 1024$. Note that density variance and χ are output every 10 s for the high resolution case, and every 2 s for the base case whilst ϵ and KE are output every simulation time step. Inset to panel *c* zooms into the region marked by the box.

Appendix A. Grid sensitivity

Grid sensitivity simulations with $Nz = 256$, $Nz = 512$ and $Nz = 1024$ were carried out between $t = 290$ and 650 s. Simulations with $Nz = 256$ rapidly diverge from the base simulation ($Nz = 512$) due to numerical instability that arise from insufficient diffusion at low grid resolutions, indicating lower grid resolutions are unsuitable. Simulations with $Nz = 512$ and $Nz = 1024$ are compared with quantitative time series of domain-integrated density measures the density variance ($\langle \rho' \rho' \rangle$) and density variance dissipation rate ($\chi = \kappa \langle (\partial \rho' / \partial x_i)(\partial \rho' / \partial x_i) \rangle$) (figures 16*a* and 16*b*), along with kinetic measures of kinetic energy (KE) and dissipation (ϵ) (figures 16*c*, and 16*d*). The two simulations show near identical-integrated KE (within 6 %) and dissipation rates (within 20 % prior to $t = 650$ s). This error ($KE_{sim} - KE_{N_z=512}) / KE_{N_z=512}$) is minimal during early periods and only peaks during active small-scale turbulence after $t \approx 640$ s. To confirm grid sensitivity for the evolution of density (since $\mathrm{Sc} < 1$), the simulations show good agreement in domain-integrated $\langle \rho' \rho' \rangle$ and $\langle \chi \rangle$. Figure 17 qualitatively compares the two resolutions as instability is developing, and show excellent agreement in the dynamics between each simulation.

Small-scale differences between solutions emerge due to sub-grid-scale motions, where the smallest Batchelor scale ($\lambda_B = ((\nu \kappa^2)/\epsilon)^{1/4}$, where ϵ is the rate of dissipation of TKE)

https://doi.org/10.1017/jfm.2026.11840 Published online by Cambridge University Press

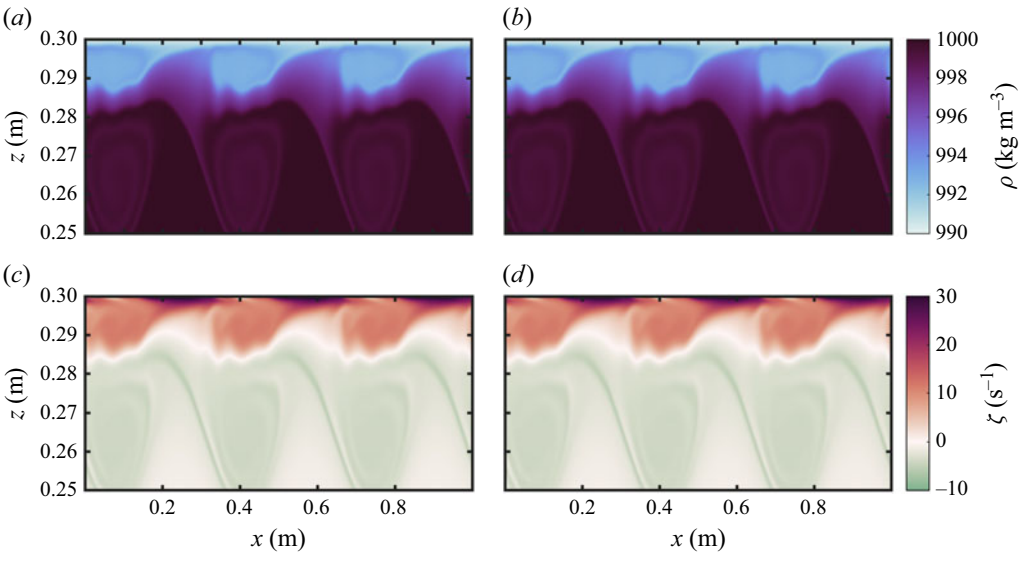


Figure 17. Qualitative comparisons of the instability dynamics for grid sensitivity of simulation ISO_Base showing ρ (a,b) and ζ (c,d) for the base case (left) and double resolution case (right) for $t = 610$ s.

decreases to approximately 20 % of the vertical grid size during the most energetic periods of flow evolution. Despite this, our simulations demonstrate only a small degree of mesh dependence. Given our primary focus is the development of instability (figure 16*c–f*), we deem these grid resolutions appropriate.

Appendix B. Perturbed simulations

In order to assess the ability of the flow to transition to an unstable state at the points identified by the LSA, two versions of ISO_Base simulation were restarted with added perturbations representing the dominant unstable mode identified via LSA, as discussed in §§ 2.3 and 3.2.1. Each field was re-initialised to one dimensional mean profiles with 2-D structure arising entirely from the added perturbations

$$u(x, z) = \langle (u(x, z)) \rangle_x + u', \tag{B1}$$

$$w(x, z) = w', \tag{B2}$$

$$\rho(x, z) = \langle (\rho(x, z)) \rangle_x + \rho'. \tag{B3}$$

The amplitude of the perturbations for each field (B, $\boldsymbol{u}$) was set to 1 % of the magnitude of that field in the original profiles. One simulation (ISO_Base+LSA_t340) was initialised from profiles at $t = 340$ s, using the dominant mode from $t = 340$ s, to represent the scenario predicted from figure 4, where the flow becomes unstable at this time. A further simulation (ISO_Base_LSA_t300) was initialised from simulation profiles at $t = 300$ s, using the mode from this same time with the wavenumber matching the dominant mode at $t = 340$ s (since there is no dominant or unstable mode at this earlier time).

In ISO_Base+LSA_340, the flow immediately becomes unstable as a result of the perturbation (figure 4*b*), evolving in a near-identical manner to ISO_Base at the later time steps (figure 18*j–l*). It is notable that the evolution of the flow is slower, as predicted by the slower σ at earlier times (figure 4). In ISO_Base+LSA_300 there is an initial decay of the perturbation between $t = 300$ and 340 s due to dissipation. When the flow becomes

https://doi.org/10.1017/jfm.2026.11840 Published online by Cambridge University Press

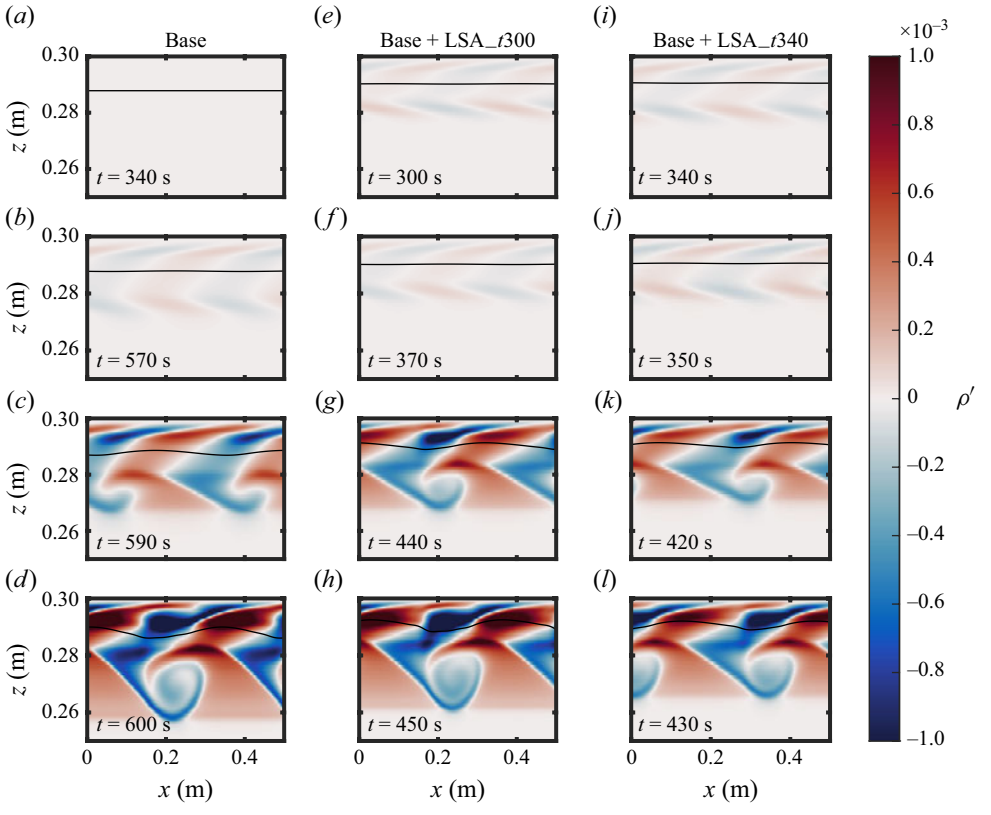


Figure 18. The evolution of perturbations in the density field for simulations ISO_Base (left), ISO_Base+LSA_t300 (centre) and ISO_Base+LSA_t340 (right). Top panels indicate the initial state with seeded perturbations visible in (*e*) and (*i*), the second row shows the emergence of the unstable mode (as in figure 9d) with the lower two panels showing the emergence and evolution of the overturning structures. Note the time intervals are not necessarily equal between simulations, and the x-axis is cropped for clarity.

unstable, the instability is slower to grow owing to a smaller initial state at the point of instability, but nonetheless evolves in the same manner as ISO_Base+LSA_340 and ISO_Base (figure 18*e–h*).

Appendix C. Wave interaction interpretation of instability applied to the compound instability

Using the interpretation of stratified shear instability as interacting vorticity and gravity waves, the fundamental tendency of this flow to go unstable is analysed, and contrasted with the inherently stable jet flow discussed in Smyth & Carpenter (2019). To simplify this analysis for a fundamental overview of the instability, the flow is reduced to a jet flow, symmetric about the velocity maximum and far from boundaries (figure 19*a*). Each of those assumptions is likely to impact the exact dynamics observed.

The wave field diagram (figure 19) shows potential interactions between the four interfaces (three vorticity interfaces, one buoyancy interface) in a piecewise profile representative of these flows. Following Lloyd & Dorrell (2024), the coincident density and buoyancy interface at the mid-depth forms a combined vorticity-gravity wave, and hereafter is considered a single interface. The analysis shows two pairs of interactions between waves, firstly the lower vorticity interface forms a resonant interaction with the

https://doi.org/10.1017/jfm.2026.11840 Published online by Cambridge University Press

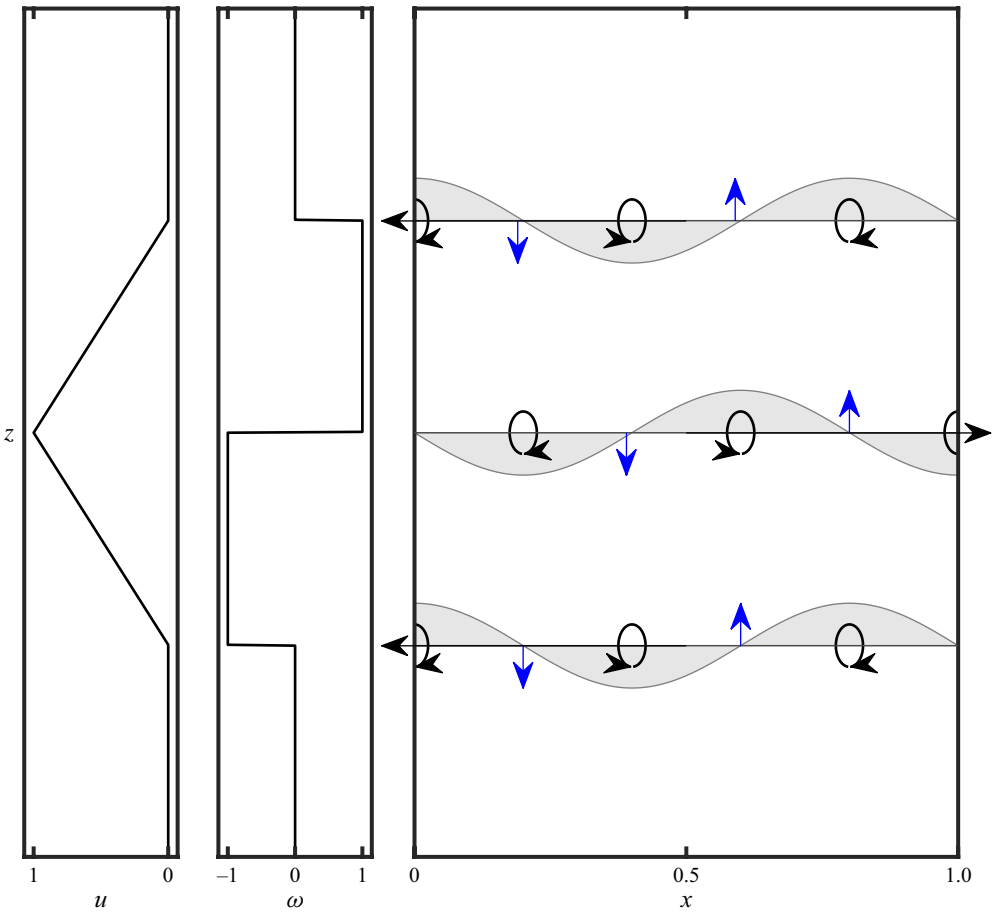


Figure 19. Wavefield diagram for a stratified jet system. Left panel is streamwise velocity profile, centre is vorticity, right is a representation of the waves at each interface, marked on with intrinsic propagation directions, a general sense of the anomaly in flow rotation (vorticity, reduced to $\mathrm{d}u/\mathrm{d}z$ for a 1-D flow), and vertical velocity perturbation at the nodes.

central vorticity-gravity wave, where the nodes of maximum vertical velocity perturbation are able to coincide with sympathetic peaks and troughs in the wave, acting to amplify them (i.e. the Rayleigh condition that there exists an inflection point somewhere in the flow (Smyth & Carpenter 2019) is met for this interaction). The intrinsic direction of propagation for the lower vorticity wave is left, whilst the intrinsic direction of propagation for the middle vorticity wave is right, the resonant internal gravity wave is assumed to take this same propagation direction (and is the direction used to identify resonance), and so this pair of interfaces matches the Fjørtoft condition that, somewhere in the flow, the second derivative of velocity is of the opposite sign to the velocity (Smyth & Carpenter 2019). In much the same manner, the upper vorticity interface and mid vorticity-gravity interface meet both the Rayleigh condition and Fjørtoft condition, overall indicating the susceptibility in qualitative terms for this flow to become unstable with the vorticity-gravity wave forming interactions with each of the outer vorticity interfaces.

The nature of the paired interactions, each being between an internal gravity interface and a vorticity interface, indicates that the flow falls within the broad categorisation of HWI, however, such a categorisation is only relevant for this symmetric form.

https://doi.org/10.1017/jfm.2026.11840 Published online by Cambridge University Press

References

Alexakis, A. 2007 Marginally unstable Holmboe modes. *Phys. Fluids* **19** (5), 054105.

Anselin, J., Holland, P.R., Jenkins, A. & Taylor, J.R. 2024 Ice base slope effects on the turbulent ice shelf-ocean boundary current. *J. Phys. Oceanogr.* **54** (7), 1545–1562.

Atoufi, A., Zhu, L., Lefauve, A., Taylor, J.R., Kerswell, R.R., Dalziel, S.B., Lawrence, G.A. & Linden, P.F. 2023 Stratified inclined duct: two-layer hydraulics and instabilities. *J. Fluid Mech.* **977**, A25.

Baglaenko, A. 2016 The effects of confinement on Kelvin–Helmholtz billows. PhD thesis, University of Waterloo.

Begeman, C.B., Asay-Davis, X. & Van Roekel, L. 2022 Ice-shelf ocean boundary layer dynamics from large-eddy simulations. *The Cryosphere* **16** (1), 277–295.

Cantero, M.I., Balachandar, S., Cantelli, A., Pirmez, C. & Parker, G. 2009 Turbidity current with a roof: direct numerical simulation of self-stratified turbulent channel flow driven by suspended sediment. *J. Geophys. Res.: Oceans* **114** (C3), C03008.

Carey, V.P. & Gebhart, B. 1981 Visualization of the flow adjacent to a vertical ice surface melting in cold pure water. *J. Fluid Mech.* **107**, 37–55.

Carpenter, J.R., Balmforth, N.J. & Lawrence, G.A. 2010*a* Identifying unstable modes in stratified shear layers. *Phys. Fluids* **22** (5), 054104.

Carpenter, J.R., Tedford, E.W., Rahmani, M. & Lawrence, G.A. 2010*a* Holmboe wave fields in simulation and experiment. *J. Fluid Mech.* **648**, 205–223.

Caulfield, C.P., Peltier, W.R., Yoshida, S. & Ohtani, M. 1995 An experimental investigation of the instability of a shear flow with multilayered density stratification. *Phys. Fluids* **7** (12), 3028–3041.

Cenedese, C. & Gatto, V.M. 2016 Impact of a localized source of subglacial discharge on the heat flux and submarine melting of a tidewater glacier: a laboratory study. *J. Phys. Oceanogr.* **46** (10), 3155–3163.

Davis, P.E.D., *et al.* 2023 Suppressed basal melting in the eastern Thwaites Glacier grounding zone. *Nature* **614** (7948), 479–485.

Davis, P.E.D. & Nicholls, K.W. 2019 Turbulence observations beneath Larsen C Ice Shelf, Antarctica. *J. Geophys. Res.: Oceans* **124** (8), 5529–5550.

Deepwell, D., Stastna, M., Carr, M. & Davies, P.A. 2017 Interaction of a mode-2 internal solitary wave with narrow isolated topography. *Phys. Fluids* **29** (7), 076601.

Depoorter, M.A., Bamber, J.L., Griggs, J.A., Lenaerts, J.T.M., Ligtenberg, S.R.M., van den Broeke, M.R. & Moholdt, G. 2013 Calving fluxes and basal melt rates of Antarctic ice shelves. *Nature* **502** (7469), 89–92.

Drazin, P.G. & Reid, W.H. 2004 *Hydrodynamic Stability*, Cambridge Mathematical Library, vol. 1, 2nd edn. Cambridge University Press.

Eaves, T.S. & Balmforth, N.J. 2019 Instability of sheared density interfaces. *J. Fluid Mech.* **860**, 145–171.

Edwards, T.L., *et al.* 2021 Projected land ice contributions to twenty-first-century sea level rise. *Nature* **593** (7857), 74–82.

Fricker, H.A., Galton-Fenzi, B.K., Walker, C.C., Freer, B.I.D., Padman, L. & DeConto, R. 2025 Antarctica in 2025: drivers of deep uncertainty in projected ice loss. *Science* **387** (6734), 601–609.

Fürst, J.J., Durand, G., Gillet-Chaulet, F., Tavard, L., Rankl, M., Braun, M. & Gagliardini, O. 2016 The safety band of Antarctic ice shelves. *Nat. Clim. Change* **6** (5), 479–482.

Gayen, B., Griffiths, R.W. & Kerr, R.C. 2016 Simulation of convection at a vertical ice face dissolving into saline water. *J. Fluid Mech.* **798**, 284–298.

Greene, C.A., Gardner, A.S., Schlegel, N.-J. & Fraser, A.D. 2022 Antarctic calving loss rivals ice-shelf thinning. *Nature* **609** (7929), 948–953.

Harnanan, S., Stastna, M. & Soontiens, N. 2017 The effects of near-bottom stratification on internal wave induced instabilities in the boundary layer. *Phys. Fluids* **29** (1), 016602.

Hartharn-Evans, S.G., Carr, M., Stastna, M. & Davies, P.A. 2022 Stratification effects on shoaling internal solitary waves. *J. Fluid Mech.* **933**, A19.

Helmholtz 1868 XLIII. On discontinuous movements of fluids. *Lond. Edinb. Dublin Phil. Mag. J. Sci.* **36** (244), 337–346.

Hill, E.A., Rosier, S.H.R., Gudmundsson, G.H. & Collins, M. 2021 Quantifying the potential future contribution to global mean sea level from the Filchner–Ronne basin, Antarctica. *Cryosphere* **15** (10), 4675–4702.

Holmboe, J. 1962 On the behavior of symmetric waves in stratified shear layers. *Geofysiske Publikasjoner* **24**, 67–113.

Holt, J.T. 1998 Experiments on Kelvin–Helmholtz billows influenced by boundaries. *Geophys. Astrophys. Fluid Dyn.* **89** (3-4), 205–233.

https://doi.org/10.1017/jfm.2026.11840 Published online by Cambridge University Press

HOWLAND, C.J., TAYLOR, J.R. & CAULFIELD, C.P. 2018 Testing linear marginal stability in stratified shear layers. *J. Fluid Mech.* **839**, R4.
ILLINGWORTH, C.R. 1950 Unsteady laminar flow of gas near an infinite flat plate. *Math. Proc. Camb.* **46** (4), 603–613.
JENKINS, A. 1991 A one-dimensional model of ice shelf-ocean interaction. *J. Geophys. Res.: Oceans* **96** (C11), 20671–20677.
JENKINS, A. 2016 A simple model of the ice shelf–Ocean boundary layer and current. *J. Phys. Oceanogr.* **46** (6), 1785–1803.
JENKINS, A. 2021 Shear, stability, and mixing within the ice shelf–ocean boundary current. *J. Phys. Oceanogr.* **51** (7), 2129–2148.
KE, J., WILLIAMSON, N., ARMFIELD, S.W. & KOMIYA, A. 2023 The turbulence development of a vertical natural convection boundary layer. *J. Fluid Mech.* **964**, A24.
KE, J., WILLIAMSON, N., ARMFIELD, S.W., MCBAIN, G.D. & NORRIS, S.E. 2019 Stability of a temporally evolving natural convection boundary layer on an isothermal wall. *J. Fluid Mech.* **877**, 1163–1185.
KELVIN, L.W. 1871 XLVI. Hydrokinetic solutions and observations. *Lond. Edinb. Dublin Phil. Mag. J. Sci.* **42** (281), 362–377.
KERR, R.C. & MCCONNOCHIE, C.D. 2015 Dissolution of a vertical solid surface by turbulent compositional convection. *J. Fluid Mech.* **765**, 211–228.
LIAN, Q., SMYTH, W.D. & LIU, Z. 2020 Numerical computation of instabilities and internal waves from in situ measurements via the viscous Taylor–Goldstein problem. *J. Atmos. Ocean. Technol.* **37** (5), 759–776.
LIU, C.-L., KAMINSKI, A.K. & SMYTH, W.D. 2023 The effects of boundary proximity on Kelvin–Helmholtz instability and turbulence. *J. Fluid Mech.* **966**, A2.
LIU, Z., THORPE, S.A. & SMYTH, W.D. 2012 Instability and hydraulics of turbulent stratified shear flows. *J. Fluid Mech.* **695**, 235–256.
LLOYD, C.J. & DORRELL, R.M. 2024 Linear dynamics in turbulent stratified plane Poiseuille flow. *J. Fluid Mech.* **999**, A104.
LLOYD, C., DORRELL, R. & CAULFIELD, C.-C. 2022 The coupled dynamics of internal waves and hairpin vortices in stratified plane Poiseuille flow. *J. Fluid Mech.* **934**, A10.
MACAYEAL, D.R. 1985 Evolution of tidally triggered meltwater plumes below ice shelves. In *Oceanology of the Antarctic Continental Shelf* (ed. S.S. Jacobs), pp. 133–143. American Geophysical Union (AGU).
MCCONNOCHIE, C.D. & KERR, R.C. 2018 Dissolution of a sloping solid surface by turbulent compositional convection. *J. Fluid Mech.* **846**, 563–577.
MCCUTCHAN, A.L. & JOHNSON, B.A. 2022 Laboratory experiments on ice melting: a need for understanding dynamics at the ice-water interface. *J. Mar. Sci. Engng* **10** (8), 1008.
MIDDLETON, L., DAVIS, P.E.D., TAYLOR, J.R. & NICHOLLS, K.W. 2022 Double diffusion As a driver of turbulence in the stratified boundary layer beneath George VI Ice Shelf. *Geophys. Res. Lett.* **49** (5), e2021GL096119.
MIDDLETON, L., VREUGDENHIL, C.A., HOLLAND, P.R. & TAYLOR, J.R. 2021 Numerical simulations of melt-driven double-diffusive fluxes in a turbulent boundary layer beneath an Ice Shelf. *J. Phys. Oceanogr.* **51** (2), 403–418.
MILES, J.W. 1961 On the stability of heterogeneous shear flows. *J. Fluid Mech.* **10** (4), 496–508.
MONDAL, M., GAYEN, B., GRIFFITHS, R.W. & KERR, R.C. 2019 Ablation of sloping ice faces into polar seawater. *J. Fluid Mech.* **863**, 545–571.
NAYAR, K.G., SHARQAWY, M.H., BANCHIK, L.D., LIENHARD, V. & JOHN, H. 2016 Thermophysical properties of seawater: a review and new correlations that include pressure dependence. *Desalination* **390**, 1–24.
OTOSAKA, I.N., *et al.* 2023 Mass balance of the Greenland and Antarctic ice sheets from 1992 to 2020. *Earth System Sci. Data* **15** (4), 1597–1616.
PARKER, J.P., CAULFIELD, C.P. & KERSWELL, R.R. 2020 The viscous Holmboe instability for smooth shear and density profiles. *J. Fluid Mech.* **896**, A14.
PATMORE, R.D., HOLLAND, P.R., VREUGDENHIL, C.A., JENKINS, A. & TAYLOR, J.R. 2023 Turbulence in the Ice Shelf–ocean boundary current and its sensitivity to model resolution. *J. Phys. Oceanogr.* **53** (2), 613–633.
PRITCHARD, H.D., LIGTENBERG, S.R.M., FRICKER, H.A., VAUGHAN, D.G., VAN DEN BROEKE, M.R. & PADMAN, L. 2012 Antarctic ice-sheet loss driven by basal melting of ice shelves. *Nature* **484** (7395), 502–505.
REESE, R., GUDMUNDSSON, G.H., LEVERMANN, A. & WINKELMANN, R. 2018 The far reach of ice-shelf thinning in Antarctica. *Nat. Clim. Change* **8** (1), 53–57.

https://doi.org/10.1017/jfm.2026.11840 Published online by Cambridge University Press

RIGNOT, E., JACOBS, S., MOUGINOT, J. & SCHEUCHL, B. 2013 Ice-shelf melting around Antarctica. *Science* **341** (6143), 266–270.
ROSEVEAR, M., GALTON-FENZI, B. & STEVENS, C. 2022 Evaluation of basal melting parameterisations using in situ ocean and melting observations from the Amery Ice Shelf, East Antarctica. *Ocean Sci.* **18** (4), 1109–1130.
ROSEVEAR, M.G., GAYEN, B. & GALTON-FENZI, B.K. 2021 The role of double-diffusive convection in basal melting of Antarctic ice shelves. *Proc. Natl Acad. Sci.* **118** (6), e2007541118.
SALEHIPOUR, H., PELTIER, W.R. & CAULFIELD, C.P. 2018 Self-organized criticality of turbulence in strongly stratified mixing layers. *J. Fluid Mech.* **856**, 228–256.
SCHETZ, J.A. & EICHHORN, R. 1962 Unsteady natural convection in the vicinity of a doubly infinite vertical plate. *J. Heat Transfer* **84** (4), 334–338.
SCHMIDT, B.E., *et al.* 2023 Heterogeneous melting near the Thwaites Glacier grounding line. *Nature* **614** (7948), 471–478.
SHEPHERD, A., *et al.* 2018 Mass balance of the Antarctic Ice Sheet from 1992 to 2017. *Nature* **558** (7709), 219–222.
SMITH, K.M., CAULFIELD, C.P. & TAYLOR, J.R. 2021 Turbulence in forced stratified shear flows. *J. Fluid Mech.* **910**, A42.
SMYTH, W.D. & CARPENTER, J.R. 2019 *Instability in Geophysical Flows*. Cambridge University Press.
SMYTH, W.D., NASH, J.D. & MOUM, J.N. 2019 Self-organized criticality in geophysical turbulence. *Sci. Rep.-UK* **9** (1), 3747.
SPINS. SPINS user guide – fluids wiki. Available at: https://wiki.math.uwaterloo.ca/fluidswiki/index.php?title=SPINS_User_Guide .
STASTNA, M., BHAVSAR, K., HARTHARN-EVANS, S. & CASTRO-FOLKER, N. 2025 The three-dimensional state of stratified shear instability in cold water. *Phys. Fluids* **37** (5), 054112.
SUBICH, C.J., LAMB, K.G. & STASTNA, M. 2013 Simulation of the Navier–Stokes equations in three dimensions with a spectral collocation method. *Intl J. Numer. Meth. Flow* **73** (2), 103–129.
TAYLOR, G.I. 1931 Effect of variation in density on the stability of superposed streams of fluid. *Proc. R. Soc. Lond. Ser. A Contain. Pap. Math. Phys. Charact.* **132** (820), 499–523.
VIEWEG, P.P. & CAULFIELD, C.-C.P. 2026 Anisotropy of emergent large-scale dynamics in forced stratified shear flows. *J. Fluid Mech.* **1029**, A7.
VREUGDENHIL, C.A. & TAYLOR, J.R. 2019 Stratification effects in the turbulent boundary layer beneath a melting ice shelf: insights from resolved large-eddy simulations. *J. Phys. Oceanogr.* **49** (7), 1905–1925.
VREUGDENHIL, C.A., TAYLOR, J.R., DAVIS, P.E.D., NICHOLLS, K.W., HOLLAND, P.R. & JENKINS, A. 2022 The ocean boundary layer beneath Larsen C ice shelf: insights from large-eddy simulations with a near-wall model. *J. Phys. Oceanogr.* **52** (8), 1903–1926.
WELLS, M., CENEDESE, C. & CAULFIELD, C.P. 2010 The relationship between flux coefficient and entrainment ratio in density currents. *J. Phys. Oceanogr.* **40** (12), 2713–2727.
WINTERS, K.B., LOMBARD, P.N., RILEY, J.J. & D'ASARO, E.A. 1995 Available potential energy and mixing in density-stratified fluids. *J. Fluid Mech.* **289** (C5), 115–128.
ZHOU, Q. 2022 Threshold behavior of local gradient Richardson number in strongly stratified nonequilibrium turbulence. *Phys. Rev. Fluids* **7** (10), 104802.
ZHU, L., ATOUFI, A., LEFAUVE, A., KERSWELL, R.R. & LINDEN, P.F. 2024 Long-wave instabilities of sloping stratified exchange flows. *J. Fluid Mech.* **983**, A12.

https://doi.org/10.1017/jfm.2026.11840 Published online by Cambridge University Press